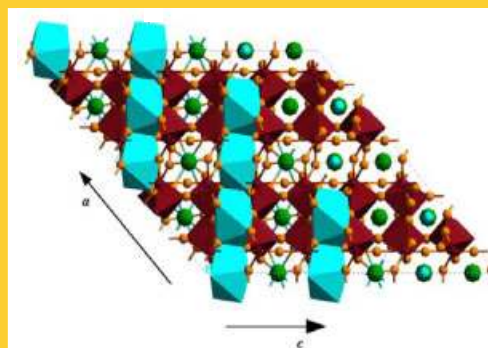


**Abstract:** High-quality crystals of monoclinic  $\text{KLu}(\text{WO}_4)_2$ , shortly KLuW, were grown with sizes sufficient for its characterization and substantial progress was achieved in the field of spectroscopy and laser operation with  $\text{Yb}^{3+}$ - and  $\text{Tm}^{3+}$ -doping. We review the growth methodology for bulk KLuW and epitaxial layers, its structural, thermo-mechanical, and optical properties, the  $\text{Yb}^{3+}$  and  $\text{Tm}^{3+}$  spectroscopy, and present laser results obtained in several operational regimes both with Ti:sapphire and direct diode laser pumping using InGaAs and AlGaAs diodes near 980 and 800 nm, respectively. The slope efficiencies with respect to the absorbed pump power achieved with continuous-wave (CW) bulk and epitaxial Yb:KLuW lasers under Ti:sapphire laser pumping were  $\approx 57$  and  $\approx 66\%$ , respectively. Output powers as high as 3.28 W were obtained with diode pumping in a simple two-mirror cavity where the slope efficiency with respect to the incident pump power reached  $\approx 78\%$ . Passively Q-switched laser operation of bulk Yb:KLuW was realized with a Cr:YAG saturable absorber resulting in oscillation at  $\approx 1031$  nm with a repetition rate of 28 kHz and simultaneous Raman conversion to  $\approx 1138$  nm with maximum energies of 32.4 and 14.4  $\mu\text{J}$ , respectively. The corresponding pulse durations were 1.41 and 0.71 ns. Passive mode-locking by a semiconductor saturable absorber mirror (SESAM) produced bandwidth-limited pulses with duration of 81 fs (1046 nm, 95 MHz) and 114 fs (1030 nm, 101 MHz) for bulk and epitaxial



Projection of the  $\text{KLu}(\text{WO}_4)_2$  structure parallel to the  $b$  crystallographic direction [010].

Yb:KLuW lasers, respectively. Slope efficiency as high as 69% with respect to the absorbed power and an output power of 4 W at 1950 nm were achieved with a diode-pumped Tm:KLuW laser. The slope efficiency reached with an epitaxial Tm:KLuW laser under Ti:sapphire laser pumping was 64 %. The tunability achieved with bulk and epitaxial Tm:KLuW lasers extended from 1800 to 1987 nm and from 1894 to 2039 nm, respectively.

© 2007 by WILEY-VCH Verlag GmbH & Co.KGaA, Weinheim

## Growth and properties of $\text{KLu}(\text{WO}_4)_2$ , and novel ytterbium and thulium lasers based on this monoclinic crystalline host

Valentin Petrov<sup>1,\*</sup>, Maria Cinta Pujol<sup>2</sup>, Xavier Mateos<sup>1</sup>, Òscar Silvestre<sup>2</sup>, Simon Rivier<sup>1</sup>, Magdalena Aguiló<sup>2</sup>, Rosa Maria Solé<sup>2</sup>, Junhai Liu<sup>1</sup>, Uwe Griebner<sup>1</sup>, and Francesc Díaz<sup>2</sup>

<sup>1</sup> Max-Born-Institute for Nonlinear Optics and Ultrafast Spectroscopy, Max-Born-Str. 2A, 12489 Berlin, Germany

<sup>2</sup> Universitat Rovira i Virgili, Campus Sescelades, c/ Marcel·lí Domingo, s/n, 43007 Tarragona, Spain

Received: 10 April 2007, Accepted: 13 April 2007

Published online: 3 May 2007

**Key words:** rare earth solid state lasers, monoclinic double tungstates, crystal growth from flux, epitaxial layers, ytterbium lasers, thulium lasers, diode-pumped lasers, ultrafast lasers

**PACS:** 42.55.Rz, 42.70.Hj, 81.10.Dn, 81.15.Np, 42.55.Xi, 42.60.Pk, 42.60.Fc, 42.60.Gd, 42.65.Dr

\* Corresponding author: e-mail: petrov@mbi-berlin.de

## 1. Introduction

The main advantages of the monoclinic potassium double tungstates as laser hosts are the very high values of the absorption and emission cross sections of the rare-earth dopants, partly due to the strong anisotropy of these biaxial crystals, and the possibility to dope them with high concentration of the active ions without substantial fluorescence quenching. Information on the synthesis, crystal structure and some thermal properties of monoclinic KLu(WO<sub>4</sub>)<sub>2</sub> (KLuW), one of the optically inert compounds belonging to this class together with KY(WO<sub>4</sub>)<sub>2</sub> (KYW) and KGd(WO<sub>4</sub>)<sub>2</sub> (KGdW), appeared for the first time in 1969 [1]. Many properties of KLuW like the thermal conductivity, hardness, optical transparency, and refractive index are very similar to those of the isostructural KYW [2]. Single crystals of KLuW were used to analyze the infrared and Raman spectra [3], and efficient high-order Stokes and anti-Stokes stimulated Raman scattering (SRS) in the visible and near-infrared was observed for the two SRS-active modes at 907 and 757 cm<sup>-1</sup> [2].

Laser emission of Er:KLuW was demonstrated for the 0.85, 1.74 and 2.81 μm transitions [4], the luminescence properties and laser operation of Ho:KLuW for the 2.08 and 2.94 μm lines were also studied [5–7], but most of the spectroscopic and laser works were devoted to Nd:KLuW [7–10], where the 1.07 and 1.35 μm lines were investigated and CW generation at 1070.2 nm was achieved at room temperature with diode pumping [10], see Table 1. Recently, some additional activities were focused on the growth, spectroscopy and diode-pumped laser operation of Nd:KLuW [11–13]. However, it is known from the earlier work that KNd(WO<sub>4</sub>)<sub>2</sub> has a different structure, and Nd-doping of KLuW is limited to about 3 at. % because stresses and cracks occur [8,14].

The KLuW host is actually predestined for doping with Yb because of the close ionic radii and masses of Yb and Lu, and the close lattice parameters of the isostructural KLuW and KYb(WO<sub>4</sub>)<sub>2</sub> (KYbW) [25]. This allows high Yb-doping levels with low defect formation probability and epitaxial growth of highly absorbing films with best quality of the interface. Moreover, the Yb-dopant affects only weakly the thermal conductivity of the host. The next most suitable dopant for KLuW is Tm. In that case the two hosts KLuW and KYW have similar deviations from the isostructural KTm(WO<sub>4</sub>)<sub>2</sub>. Here we will review the growth, structure, and physical properties of KLuW, the spectroscopy of Yb<sup>3+</sup> and Tm<sup>3+</sup> in KLuW, and the laser results obtained by us with bulk and epitaxial Yb:KLuW and Tm:KLuW crystals (see Table 1). Note that more recently, KLuW was also doped with Sm [26], Dy [27], and Tb [28], as well as co-doped with Er:Yb, by the present authors and in [27], and with Yb:Tm [29], but lasing has not been demonstrated in such crystals, yet.

## 2. Crystal structure and growth of bulk and epitaxial KLuW

The structure of the low-temperature monoclinic phase of KLuW was studied as early as 1968 but the lattice parameters determined by X-ray powder diffraction were reported in the *I2/c* space group [1]. Subsequently, they were revised and refined in the *C2/c* space group, however, still using powdered crystals [14,25]. Our results derived from single-crystal X-ray diffraction data [30] are included in Table 9. Similar results with single crystals were reported also in [31]. KLuW has the structure of KYW, as the other potassium double tungstates of the heavier lanthanides starting from KSm(WO<sub>4</sub>)<sub>2</sub> (KSmW) for which the unit cell parameters and hence the interatomic distances tend to decrease with the Ln atomic number [1].

Lutetium is eightfold coordinated by oxygen atoms, forming a distorted square antiprism. The local site symmetry of the Lu<sup>3+</sup> cation is *C*<sub>2</sub> (4e Wyckoff position), and substitution by dopant ions takes place in this unique site. The LuO<sub>8</sub> polyhedra form a single zig-zag chain in the [101] direction sharing O—O edges [3.081(11) Å]. The length of these shared O—O edges increases along the KSmW-KLuW series due to the increasing positive charge of the nucleus of the Ln-element. As a consequence, the strength of one of the Lu—O bonds increases and the interatomic separation is decreased to 2.299(7) Å in comparison to the separation of 2.371(10) Å for Gd—O in KGdW [32]. The resulting degree of distortion of the LuO<sub>8</sub> coordination polyhedra calculated for the KLuW host is more than two times higher in comparison to KGdW [30].

The distances between Lu—Lu pairs are also important because they affect the energy transfer between the dopant ions. The Lu—Lu distance in the same LuO<sub>8</sub> chain parallel to the [101] direction is 4.045(3) Å. Each such lutetium polyhedra chain is surrounded by four equivalent chains, and the corresponding Lu—Lu distances are 5.982(3) Å and 6.693(3) Å. This environment is similar to that of KGdW where the corresponding Gd—Gd separations amount to 4.070(2) Å, 6.057(2) Å, and 6.804(2) Å.

The coordination figure of the tungstate anion is a distorted octahedron, WO<sub>6</sub>, (W—O distances ranging from 1.767(7) Å to 2.265(8) Å). The units W<sub>2</sub>O<sub>8</sub>, which are constituted by two distorted octahedra sharing O—O edges, form a characteristic double chain in the crystallographic *c* direction by sharing vertex O. The average W—O distance gets shorter along the KSmW-KLuW series which means decreasing distortion of the WO<sub>6</sub> octahedra leading to more compact and covalent WO<sub>6</sub> groups. As in the other monoclinic double tungstates, the alkali cation K<sup>+</sup> is twelve-coordinated by O ions, forming a distorted icosahedron. Figure 1 shows the LuO<sub>8</sub> zig-zag chains along the [101] direction and the W<sub>2</sub>O<sub>8</sub> double chains along the [001] direction.

The knowledge of the unit cell variation with doping is important e.g. for epitaxial growth of doped layers on undoped substrates or for diffusion bonding of doped and

**Table 1** Laser operation demonstrated with lanthanide (Ln) doped (activated) KLuW.

Ln <sup>3+</sup>	doping <sup>f</sup> [at. %]	polarization <sup>◇</sup>	transition	wavelength [nm]	pump	remarks*	[Ref.] (year)
Nd	3	$\perp a$	$^4F_{3/2} \rightarrow ^4I_{13/2}$	1348.2	Xe-lamp	pulsed	[7] (1979)
Nd	2	$\perp a', \perp c$	$^4F_{3/2} \rightarrow ^4I_{13/2}$	1353.3, 1355	Xe-lamp	pulsed	[8] (1983)
Nd	2	$\perp b$	$^4F_{3/2} \rightarrow ^4I_{13/2}$	1355			
Nd	3	$\perp a$	$^4F_{3/2} \rightarrow ^4I_{11/2}$	1071.4	Xe-lamp	pulsed	[7] (1979)
Nd	2	$\perp a'$	$^4F_{3/2} \rightarrow ^4I_{11/2}$	1072.1	Xe-lamp	77 and 300 K, pulsed	[8] (1983)
Nd	2	$\perp b, \perp c$	$^4F_{3/2} \rightarrow ^4I_{11/2}$	1070.1, 1070.2			
Nd	~5	NA	$^4F_{3/2} \rightarrow ^4I_{11/2}$	1070.1	pyro-lamp	quasi-CW	[9] (1983)
Nd	3	$\perp b$	$^4F_{3/2} \rightarrow ^4I_{11/2}$	1070.2	diode laser	quasi-CW, CW	[10] (1992)
Nd	3	$\perp b$	$^4F_{3/2} \rightarrow ^4I_{11/2}$	1073	diode laser	CW	[13] (2005)
Er	3, 5, 25	$\perp b, \perp c$	$^4I_{11/2} \rightarrow ^4I_{13/2}$	2809.2	Xe-lamp	pulsed	[4] (1979)
Er	3, 5	$\perp b$	$^4S_{3/2} \rightarrow ^4I_{9/2}$	1738.3			
Er	5	$\perp b$	$^4S_{3/2} \rightarrow ^4I_{13/2}$	~850			
Ho	3	$\perp c$	$^5I_7 \rightarrow ^5I_8$	2079	Xe-lamp	110 K, pulsed	[6] (1981)
Ho	3	$\perp b$	$^5I_6 \rightarrow ^5I_7$	2944.5	Xe-lamp	pulsed	[7] (1979)
Yb	5, 10	$\parallel N_m$	$^2F_{5/2} \rightarrow ^2F_{7/2}$	1033.3-1051.3	Ti:sapphire	CW	[15,16] (2004)
Yb	5	$\parallel N_m$	$^2F_{5/2} \rightarrow ^2F_{7/2}$	1041-1047	diode laser	CW	[15,16] (2004)
Yb	5	$\parallel N_m$	$^2F_{5/2} \rightarrow ^2F_{7/2}$	1039.5-1052.4	diode laser	CW	[17] (2005)
Yb	5	$\parallel N_p$	$^2F_{5/2} \rightarrow ^2F_{7/2}$	1046	Ti:sapphire	CW	[18] (2005)
Yb	5	$\parallel N_m$	$^2F_{5/2} \rightarrow ^2F_{7/2}$ 1st Stokes	1030.6 1137.6	diode laser	Q-switched + self-Raman laser	[17] (2005)
Yb	5	$\parallel N_m$	$^2F_{5/2} \rightarrow ^2F_{7/2}$	1046	Ti:sapphire	M-L, fs	[18] (2005)
Yb	5	$\parallel N_p$	$^2F_{5/2} \rightarrow ^2F_{7/2}$	1043, 1049 1053	Ti:sapphire diode laser	M-L, ps & fs, M-L, fs	[18] (2005)
Yb	10	$\parallel N_m$	$^2F_{5/2} \rightarrow ^2F_{7/2}$	1026-1040 1030	Ti:sapphire diode laser	epitaxy, CW	[19] (2005)
Yb	50	$\parallel N_m$	$^2F_{5/2} \rightarrow ^2F_{7/2}$	1032, 1046.1	Ti:sapphire	epitaxy, quasi-CW, CW	[20] (2006)
Yb	10	$\parallel N_m$	$^2F_{5/2} \rightarrow ^2F_{7/2}$	1030	Ti:sapphire	epitaxy, M-L, ps & fs	[21] (2005)
Tm	3	$\parallel N_m$	$^3F_4 \rightarrow ^3H_6$	1943-1975	diode laser	CW	[22,23] (2006)
Tm	3, 5	$\parallel N_m$	$^3F_4 \rightarrow ^3H_6$	1917-1951 1809-1983	Ti:sapphire	CW CW-tunable	[23] (2006)
Tm	3	$\parallel N_p$	$^3F_4 \rightarrow ^3H_6$	1907-1942 1800-1987	Ti:sapphire	CW CW-tunable	
Tm	5	$\parallel N_m$	$^3F_4 \rightarrow ^3H_6$	1960-1967 1894-2039	Ti:sapphire	epitaxy, CW CW-tunable	[24] (2007)

<sup>f</sup> doping level in the solution; the data on the segregation coefficient of Nd in [11,13] is contradictory; <sup>◇</sup> the crystallographic *a'* axis (*I*2/c space group) is at  $\approx 44.7^\circ$  from the *a*-axis (*C*2/c space group); \* M-L: mode-locked; if not mentioned, the temperature is 300 K.

undoped KLuW. For Yb and Tm doping we studied the variation of the unit cell parameters of KLuW by the X-ray powder diffraction method. The samples used were grown with 10, 20, 50 and 100 at. % Yb doping and 3, 5, 7.5, 10, and 20 at. % Tm doping in the solution but the actual crystal composition, determined from electron microprobe analysis, was used to obtain the evolution of the unit cell parameters in Fig. 2 [30,33].

As could be expected, the monoclinic symmetry is maintained in all cases because KYbW and KTmW have the same structure as KLuW [1]. The unit cell parameters *a*, *b* and *c* increase and  $\beta$  remains basically constant when

the doping concentration of Yb and Tm increases. This increase is also not unexpected because the ionic radii of Tm (0.994 Å) and Yb (0.985 Å) are larger than that of Lu (0.977 Å).

Polarized infrared and Raman spectra of KLuW were measured in the past and compared with the other isostructural potassium double tungstates [3]. Due to the presence of two non-equivalent structural groups in the primitive cell, the factor group analysis predicts a total of 72 vibrations distributed among the following irreducible representations:  $17A_g + 19B_g + 17A_u + 19B_u$ . The  $A_g$  and  $B_g$  modes are Raman active, and the  $A_u$  and  $B_u$  modes are

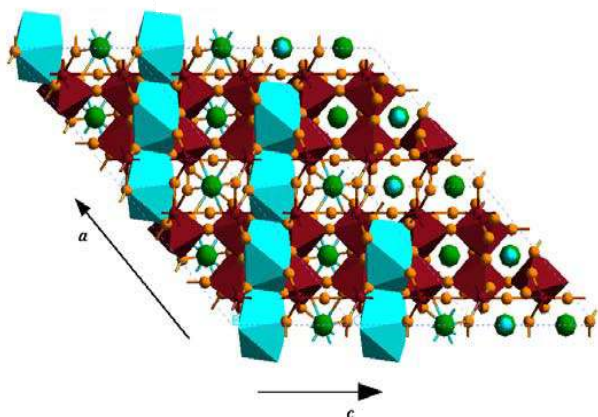


**Figure 1** Projection of the KLuW structure parallel to the *b* crystallographic direction [010].

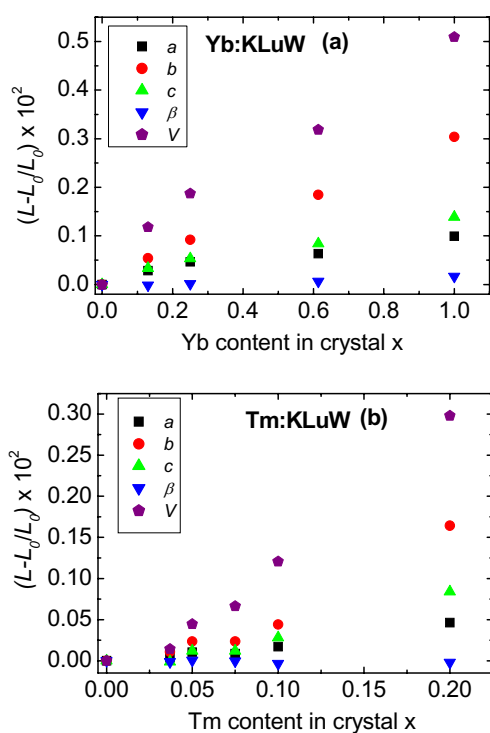


**Figure 2** Evolution of the unit cell parameters ( $L = a, b, c, \beta$ ) and the unit cell volume ( $L = V$ ) with the dopant concentration  $x$  of  $\text{KLu}_{1-x}\text{Yb}_x\text{W}$  (a) and  $\text{KLu}_{1-x}\text{Tm}_x\text{W}$  (b).

infrared active. The modes can be further subdivided into acoustic ( $T = 1A_u + 2B_u$ ), optical translational lattice modes ( $T' = 2A_g + 4B_g + 4A_u + 5B_u$ ), optical librational lattice modes ( $L = 3A_g + 3B_g$ ) and optical internal modes for the  $\text{W}_2\text{O}_8$  units (int =  $12A_g + 12B_g + 12A_u + 12B_u$ ) [34,35].

**Table 2** Vibrational frequencies for KLuW.

assignment	energy [cm <sup>-1</sup> ]
$T'(W^{6+}) / ? \nu_3^0 - \nu_3^-$	63
$T'(W^{6+}) / B_g$	<b>87</b>
$L(WO_6) * \delta(WOW) / E_g$	112
$? / E_u$	130
$\gamma(WOOW) * T'(K^+) / E_u / \nu_1 - \nu_3^0$	147
$\gamma(WOOW) * T'(K^+) / A_u$	175
$T'(Lu^{3+}) / E_g$	218
$T'(K^+) / B_g$	236
$\delta(WOOW) / ?$	289
$\gamma(WOW) / \nu_2^-$	317
$\delta(W-O) / ? \nu_2^+$	345
$\delta(W-O) / ? \nu_2^+$	350
$\delta(W-O) / ?$	381
$\nu(W-O) / \nu_4^-$	406
$\delta(WOW) / \nu_4^0$	450
$\nu(WOOW) / \nu_4^-$	535
$\nu(WOOW) * \nu(W-O) / \nu_3^-$	686
$\nu(WOOW) * \nu(W-O) / \nu_3^0$	<b>756</b>
$\nu(WOW) * \nu(W-O) / \nu_3^+$	809
$\nu(W-O) / \nu_1$	<b>908</b>
$2\nu_1 - \nu_3^0$	1063

$\nu$ : stretching mode,  $\delta$ : bending mode,  $\gamma$ : out-of-plane mode, \* coupling of the vibrations, ? unidentified

The values of the phonon energies we determined from Raman spectra recorded with single crystals of KLuW, excitation by an Ar-laser at 514 nm, and backscattering geometry, are summarized in Table 2. The labelling of the assignment of the peaks is according to the more recent classification in [34,35] and a simplified nomenclature derived from the scheelite structure [36]. Figure 3 shows a room temperature Raman spectrum recorded in the frequency range 0 to 1200 cm<sup>-1</sup>. We used here designations related to the optical indicatrix (see next section), as usual in spectroscopy. The phonons below 270 cm<sup>-1</sup> can be attributed to external lattice modes associated with translational motion of the cations of the structure ( $K^+$ ,  $Lu^{3+}$ , and  $W^{6+}$ ) and rotational motion of  $WO_6$  groups in the unit cell. The bending modes appear in the 270–460 cm<sup>-1</sup> region, and the stretching modes in the 400–1000 cm<sup>-1</sup> region. The bands in the 430–750 cm<sup>-1</sup> region, not observed for isolated  $WO_4$  tetrahedra, are related to double oxygen bridge vibrations activated when the coordination number of tungsten increases from 4 to 6 [34].



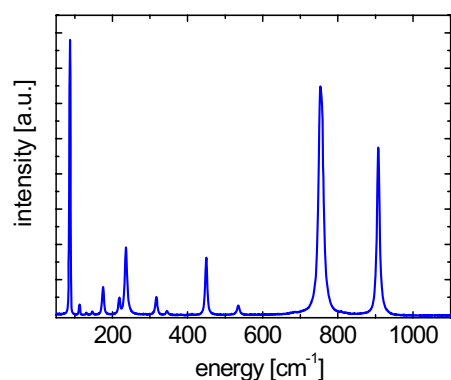


**Figure 3** Raman spectrum of KLuW:  $p(gm)\bar{p}$  geometry.

The boldface numbers in Table 2 designate the strongest Raman lines, interesting for SRS. The linewidth of the 756 and 908  $\text{cm}^{-1}$  modes is 13.7 and 8.5  $\text{cm}^{-1}$ , respectively, somewhat less than the 16.6 and 12.5  $\text{cm}^{-1}$  reported for 5 at. % Yb:KLuW in [37] (note the different frame in [37]).

A polymorphic transformation of KLuW just below the melting point of 1363 K was suggested but not resolved in [1]. Thus, the low-temperature monoclinic phase can be grown only from high-temperature solutions. Polymorphism is typical for the potassium rare-earth double tungstates, and for KLuW, orthorhombic (with layered  $\text{KY}(\text{MoO}_4)_2$  structure) and trigonal (with  $\text{KAl}(\text{MoO}_4)_2$  structure) modifications are also known [25,38,39]. The temperature of the first transition to the orthorhombic phase was given as 1293–1298 K [8,14] and that of the second transition – as just below the melting temperature of 1363 K [1,14]. The results of our differential thermal analysis are shown in Fig. 4 and included in Table 9. Whereas the slightly lower melting temperature seems to be confirmed also by analogous measurements of 5 at. % Yb-doped KLuW [40], the two phase transitions seem not to be resolved in Fig. 4 and also in [40].

We grow KLuW by the top-seeded solution growth (TSSG) slow-cooling method with a cylindrical vertical furnace as described elsewhere [41]. The composition is about 12/88 mol % solute/solvent ( $\text{K}_2\text{W}_2\text{O}_7$ ). This is the standard solvent used for KLuW [1], with the basic advantages being the absence of foreign ions, the low melting temperature, and the low viscosity during growth as a result of the higher W content [41]; another possibility is  $\text{K}_2\text{WO}_4$  [1,11,12] but it does not ensure good homogenisation of the solution and is more prone to evaporation.

The solubility curve of monoclinic KLuW in  $\text{K}_2\text{W}_2\text{O}_7$  is shown in Fig. 5. The limits of the solubility curve are given by the properties of this binary system. At a solute content of  $\approx 54$  mol %, the phase that crystallises first when decreasing the temperature should be the orthorhombic one. The lower limit of  $\approx 5$  mol % for the solute is related to the economical profitability of the growth pro-

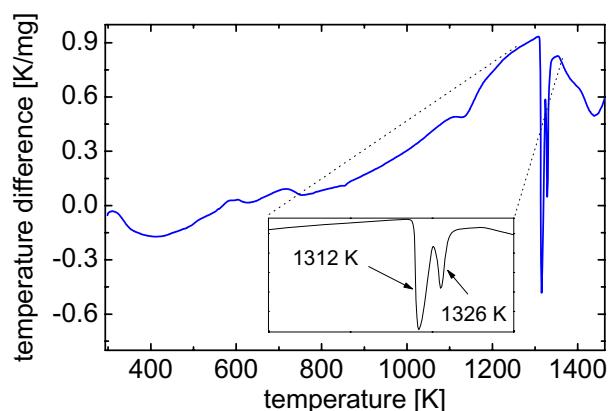


**Figure 4** Differential thermal analysis of KLuW.

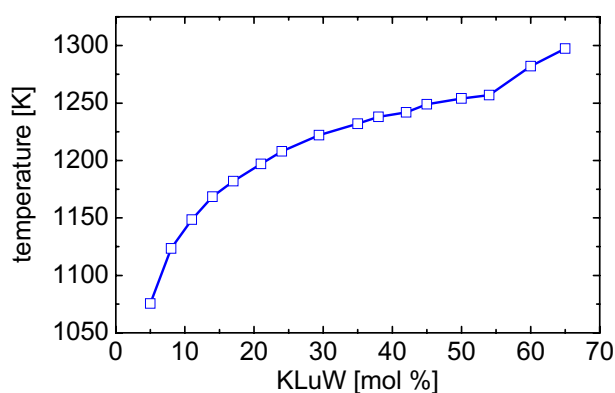


**Figure 5** Solubility curve of KLuW in  $\text{K}_2\text{W}_2\text{O}_7$ .

cedure. Although the monoclinic phase of KLuW can be grown for solute content between 5 and 54 mol %, it is better to remain in the 5–15 mol % range where variations of the temperature lead to only small changes in the supersaturation. The growth temperature when using such solutions is 1090–1175 K which means relatively low economical cost of the growth procedure.

The knowledge of some physical properties of the growth solutions, such as density, surface tension, viscosity and thermal conductivity is of great importance for optimizing the conditions for single crystal growth by the TSSG method. In order to determine the optimum conditions for the growth of single crystals of KLuW, the temperature dependence of the density, surface tension and viscosity was studied for a solution of  $\text{KLuW}/\text{K}_2\text{W}_2\text{O}_7 = 12/88$  mol %.

The density measurements were performed by the Archimedean method based on two bobs with identical supports. The surface tension was obtained by the dipping cylinder method, based on the measurement of the maximum pull exerted on the lower open end of a Pt/Pt-10%Rh cylinder, just before the meniscus is broken. The

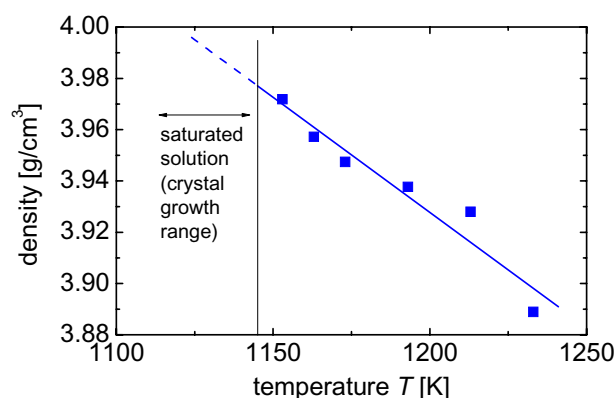


**Figure 6** Thermal evolution of the density of the KLuW/K<sub>2</sub>W<sub>2</sub>O<sub>7</sub> solution for 12 mol % KLuW.

weight measurements, made with the same balance, were recorded with a frequency of 1 Hz while the crucible was lowered at a rate of 1 cm/min. The viscosity measurements were performed by the damping method. An open-end cylinder of Pt/Pt-10%Rh was immersed in the solution, suspended by a torsion wire. The oscillation attenuation was observed by means of a laser beam reflected on a mirror located in the axial plane.

Figures 6 and 7 show the density, surface tension and viscosity of the solution versus temperature. As can be seen, the density and surface tension decrease linearly with increasing temperature. The viscosity also decreases with the temperature having a similar behaviour.

Taking into account the solubility curve of KLuW in K<sub>2</sub>W<sub>2</sub>O<sub>7</sub>, the saturation temperature  $T_S$  of the solution was estimated to be about 1145 K. All measurements were performed above this temperature in order to avoid crystallization although the aim was to determine the physical properties of the solution in the temperature range where the crystal growth takes place. The cooling interval for the growth of bulk KLuW crystals is about 20 K. The extrapolation of the obtained curves into this range leads to the following mean values for the density, surface tension and viscosity, respectively: 3.98 g/cm<sup>3</sup>, 108.8 dyn/cm and 38.8 cP.

The crystals are grown in Pt crucibles using K<sub>2</sub>CO<sub>3</sub>, WO<sub>3</sub>, and Ln<sub>2</sub>O<sub>3</sub> (Ln = Lu, Yb, Tm) as starting materials, with 99.9% purity. A KLuW seed oriented along the *b*-crystallographic axis is attached to a Pt holder rotating at 40 rpm. The temperature gradient in the solution is about 1 K/cm in the vertical and radial directions with the bottom and walls being hotter. The growth occurs as a result of supersaturation when cooling below the saturation temperature which depends on the flux composition and slightly increases with the doping level. The cooling rate during growth varies between 0.1 and 0.3 K/h, depending on the crystal size and the doping level. Finally, the grown crystals are removed slowly from the solution and cooled at a rate of 15–25 K/h, slightly above the surface.

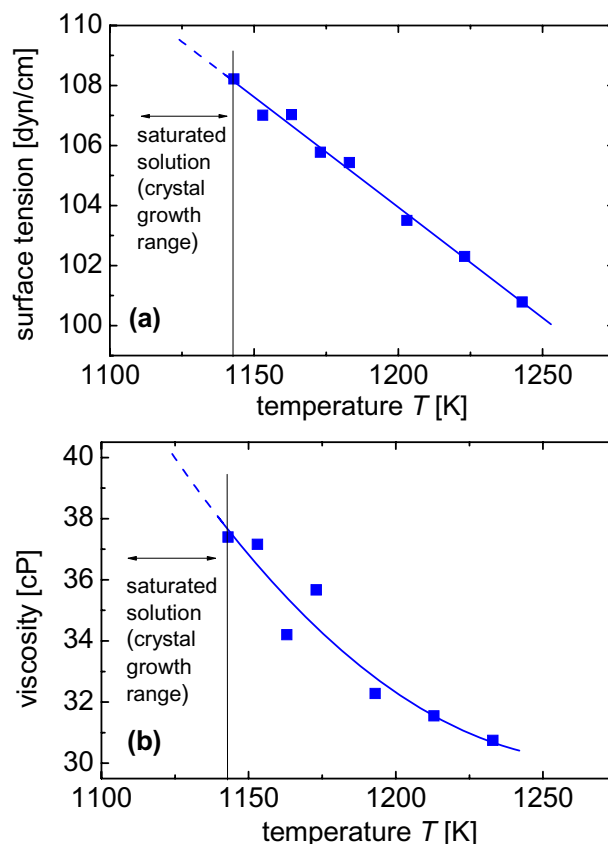


**Figure 7** Thermal evolution of the surface tension (a) and the dynamic viscosity (b) of the KLuW/K<sub>2</sub>W<sub>2</sub>O<sub>7</sub> solution for 12 mol % KLuW.

Figure 8 shows the distribution of Yb in a single crystal of Yb:KLuW. The segregation coefficient  $K_{Yb}$  or  $K_{Tm}$ , which is normally close to unity, ensures rather homogeneous distribution of the doping ions, both Yb and Tm,

**Table 3** Crystal growth data for Yb-doped KLuW. A: Yb substitution in solution relative to Lu [at. %], B: Cooling rate during growth [K/h], C: Cooling interval [K], D: Crystal weight [g], E: Growth rate [ $10^{-4}$  g/h], G, H, and I: Crystal dimensions [mm] along the *c*, *a*\*, and *b* crystallographic directions, respectively.

A	B	C	D	E	G	H	I	$K_{Yb}$
0.5	0.1	18.5	4.3082	232	9.5	6.6	4.7	1.39
1.0	0.1	18.9	4.5719	242	12.2	11.8	7.8	1.37
1.5	0.1	18.8	4.2797	228	19.5	8.4	6.3	1.61
3	0.1	17.6	3.3310	189	10.0	10.9	9.3	1.45
5	0.1	17.2	3.4670	202	10.1	11.6	8.0	1.37
10	0.2	20	2.7293	273	12.1	9.5	6.9	1.30
25	0.15	20	2.6929	202	13.5	8.4	6.3	1.24
50	0.2	20	8.550	814	18	13	10.6	1.22

**Table 4** Crystal growth data for Tm-doped KLuW. A: Tm substitution in solution relative to Lu [at. %], B: Cooling rate during growth [K/h], C: Cooling interval [K], D: Crystal weight [g], E: Growth rate [ $10^{-4}$  g/h], G, H, and I: Crystal dimensions [mm] along the  $c$ ,  $a^*$ , and  $b$  crystallographic directions, respectively.

A	B	C	D	E	G	H	I	$K_{Tm}$
0.5	0.2	20	3.9716	397	14.1	11.1	7.47	1.87
1	0.2	20	3.6277	362	14.3	10.11	5.4	1.17
3	0.1	20	5.6229	281	11.32	9.28	7.15	1.23
5	0.1	20	4.9860	249	15.2	10.4	7.5	0.997

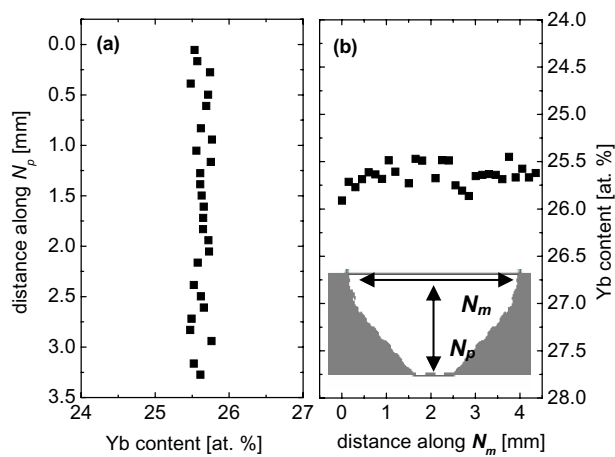


**Figure 8** Yb distribution profile along the  $N_p \equiv b$  (a) and  $N_m$  (b) principal optical axes of  $KLu_{0.745}Yb_{0.255}W$ .

within the crystal. Typical sizes and weights of the grown crystals are about one cubic centimetre (see Fig. 9) and several grams. Tables 3 and 4 present data related to the growth parameters of Yb- and Tm-doped KLuW using  $b$ -oriented seeds. Some attempts were performed also using  $c$ -oriented seeds. Macro-defect free single crystals of KLuW were obtained also in this case but the average growth rate was slightly lower than for  $b$ -oriented seeds.

The morphology of the grown crystals is similar to that we observed for other isostructural compounds of the same type [32,41,42], with the developed faces being  $\{110\}$ ,  $\{\bar{1}11\}$ ,  $\{010\}$  and  $\{310\}$ , see Fig. 9. The external manifestation of the  $\{010\}$  face in these materials is important as a structural reference in order to prepare samples for characterization purposes or laser applications. Using the same growth procedure we observed that the  $\{010\}$  face tends to decrease its area with increasing Ln atomic number which means that the growth rate of this face is increasing [30,32,42].

According to the Hartman-Perdok theory [43], the crystal morphology is governed by the presence of periodic bond chains (PBCs) and we studied the morphology of KLuW from this point of view. Table 5 shows the

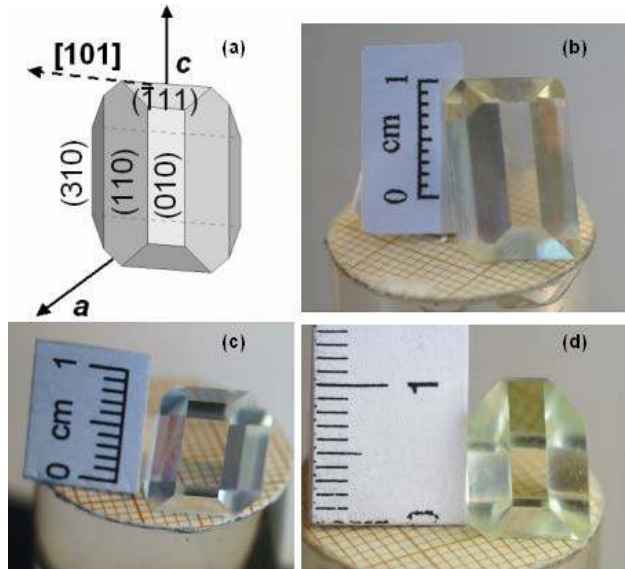


**Figure 9** Morphology (a) and single crystals of undoped (b), 5 at. % Yb-doped (c) and 3 at. % Tm-doped (d) KLuW.

**Table 5** Strongest PBCs of monoclinic KLuW and their periods.

$\langle uvw \rangle$	PBC period [nm]
$1/2 \langle 110 \rangle$	0.7315
$\langle 001 \rangle$	0.7487
$1/2 \langle 112 \rangle$	0.7647
$\langle 101 \rangle$	0.8042

**Table 6** Observed faces  $\{hkl\}$  on the grown KLuW crystals, their interplanar  $d_{hkl}$ -spacings, and the PBCs parallel to them.

$\{hkl\}$	$d_{hkl}$ [nm]	$\langle uvw \rangle$	PBCs
110	0.6308	$[0\ 0\ 1]$	$[\bar{1}\ 1\ 0]$ $[1\ \bar{1}\ 2]$
$\bar{1}11$	0.6028	$[1\ 0\ 1]$	$[\bar{1}\ \bar{1}\ 0]$ $[1\ \bar{1}\ 2]$
010	0.5107	$[0\ 0\ 1]$	$[1\ 0\ 1]$ $[1\ \bar{1}\ 2]$
021	0.3797		$[\bar{1}\ \bar{1}\ 0]$
$\bar{2}21$	0.3669		
130	0.3140	$[0\ 0\ 1]$	
310	0.2586	$[0\ 0\ 1]$	

four strongest PBCs which are simultaneously the PBCs with the shortest repetition periods in the KLuW structure. Table 6 lists the faces observed on the KLuW crystals obtained in our experiments and shows the PBCs parallel to them. The growth rate of a  $\{hkl\}$  form is inversely proportional to the interplanar spacing  $d_{hkl}$ , also included in Table 6. Faces with lower growth rate are more important for the morphology of the crystal because faces which grow faster tend to be less developed.

The interplanar  $d_{hkl}$ -spacings, the shortest periods of the PBCs, and the unit cell parameters are affected by the smaller radius of the Lu-ion and some trends can be observed when comparing to other isostructural hosts like KGdW: Thus, the ratio  $d_{010}/d_{110}$  is somewhat smaller for KLuW in comparison to KGdW. This ratio can be associated with the external manifestation of the {010} face in competition with the {110} face – its decrease will be expressed in the external habit of the grown crystals to have smaller area of the {010} face and larger area of the {110} face. Furthermore, from the comparison of the unit cell parameters of the monoclinic potassium double tungstates [1], it can be concluded that the relative decrease of the  $b$  parameter when the atomic number of the Ln-element increases is more pronounced than that of the  $a$  and  $c$  parameters. This affects the tendency of developing a face which is proportional to  $d_{hkl}$ . However, the slight modification in the development of the {010} face could be also related to the different physico-chemical properties of the solutions (e.g. KLuW-K<sub>2</sub>W<sub>2</sub>O<sub>7</sub> vs. KGdW-K<sub>2</sub>W<sub>2</sub>O<sub>7</sub>).

The {110},  $\{\bar{1}11\}$  and {010} faces are parallel to two or more PBCs; this agrees with the fact that these faces are well developed, i.e. they grow slowly and the mechanism of the growth is slice to slice. The {130}, {310}, {021} and  $\{\bar{2}21\}$  faces are parallel to one PBC and their growth rate is higher; hence, these faces are less developed and do not always appear. Figure 10 shows a projection parallel to [001] direction. One can see the interplanar spacing  $d_{110}$  and the corresponding PBCs [001] which are linked in the  $[\bar{1}10]$  direction. The interplanar spacing  $d_{020}$  corresponds to the form {010} which contains the [001] PBCs linked in the [101] direction. Finally the interplanar spacings  $d_{130}$  and  $d_{310}$  are associated with the forms {130} and {310}, respectively; they also contain [001] PBCs but there are no links between the PBCs. The larger the interplanar spacing of a given form {hkl}, the higher the number of PBCs that can be contained. As a consequence, the slice contains more strong bonds, the rate of growth perpendicular to the {hkl} face is smaller and the face appears more developed. Furthermore, crystals grown from  $b$ -oriented seeds have the [001] and [101] PBC directions as natural edges.

Besides some differences in the observed morphology of the grown crystals, we note that the authors of [44], see also [45,46], favour  $c$ -oriented seeds for the TSSG of KLuW because according to their experience such seeds provide superior crystal quality and higher utilization ratio.

The production of thin doped layers is important for highly absorbing materials, especially for the realization of simplified (less pump passes) versions of the thin disk laser concept [47], the power scalability of which is inversely proportional to the crystal thickness, but also in general for a better overlap with the pump beam in the case of diode pumping. The latter is relevant also to waveguide structures which can be fabricated by different techniques for refractive index manipulation: e.g. oxygen ion implantation was recently used for planar waveguide structures based on Yb:KLuW [48]. The monoclinic double tungstates are very promising for thin film laser designs

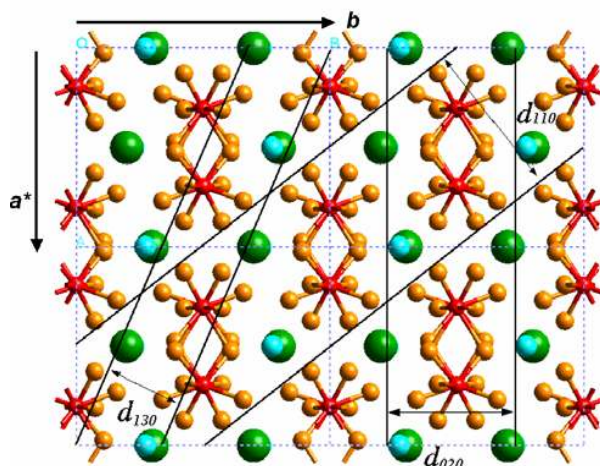


**Figure 10** Projection of the KLuW structure parallel to [001] showing the interplanar  $d_{hkl}$ -spacings of the forms {010}, {110}, {130} and {310} parallel to [001] PBCs.

**Table 7** Face area mismatch for doped KLuW layers on KLuW.

epitaxial layer	$f\{010\}$	$f\{110\}$	$f\{310\}$	$f\{\bar{1}11\}$
KLu <sub>0.88</sub> Yb <sub>0.12</sub> W	0.0739	0.0812	0.0637	0.0889
KLu <sub>0.78</sub> Yb <sub>0.22</sub> W	0.1074	0.1306	0.1034	0.1347
KLu <sub>0.48</sub> Yb <sub>0.52</sub> W	0.1436	0.2204	0.1570	0.2109
KYbW	0.2156	0.3557	0.2556	0.3248
*KLu <sub>0.97</sub> Tm <sub>0.03</sub> W	0.0689	0.0642	0.0568	0.0731
*KLu <sub>0.95</sub> Tm <sub>0.05</sub> W	0.0859	0.0868	0.0772	0.0897
*KLu <sub>0.925</sub> Tm <sub>0.075</sub> W	0.0855	0.0993	0.0776	0.1029
*KLu <sub>0.90</sub> Tm <sub>0.10</sub> W	0.1161	0.1366	0.1041	0.1402
*KLu <sub>0.80</sub> Tm <sub>0.20</sub> W	0.1984	0.2615	0.1957	0.2489

\*for Tm-doping the composition refers to the solution

just because of the high doping levels possible and the large interaction cross sections. Thus, e.g. the stoichiometric KYbW which exhibits only weak fluorescence quenching has an absorption length of only 13.3  $\mu$ m for pumping at 981 nm with polarization  $E//N_m$  [36].

We applied liquid phase epitaxy (LPE) for growth of thin Yb- or Tm-doped KLuW crystalline layers on passive KLuW substrates. KLuW is obviously the best choice for Yb-doped monoclinic composites of this type because the lattice mismatch with respect to KYbW (0.33% on the average for  $a$ ,  $b$ , and  $c$ ) is minimum [19]. Minimum mismatch means reduced stress at the layer-substrate interface. Table 7 summarizes the area mismatch for the different crystal faces defined by the expression  $f\{hkl\} = [S_L\{hkl\} - S_S\{hkl\}] / S_S\{hkl\}$  where  $S_S$  and  $S_L$  are the areas calculated from the {hkl} periodicity vectors of the substrate and the layer (Yb- or Tm-doped), respectively.

For Yb:KLuW layers, the smallest lattice mismatch when increasing the doping level occurs for the {010}



face. For Tm:KLuW layers, the smallest lattice mismatch is for the {310} face, followed by the {010} face. Since the {010} face is simultaneously a principal optical plane, as described in the next section, it is still better to orient the substrates parallel to this face.

The LPE growth technique is basically the same as for bulk crystals but the special furnace has a wide zone of uniform temperature to ensure almost vanishing temperature gradient. Also, the solvent part was increased to 93–95 mol % for better control of the growth rate in accordance with the solubility curves [19,24,49]. After homogenisation of the solution, its saturation temperature was accurately determined with *b*-oriented KLuW seeds rotating at 40 rpm. The passive substrates were *b*-cut plates which were dipped into the solution with the [001] direction perpendicular to the solution surface. Before inserting them into the furnace, the substrates were carefully cleaned, in rotation, in 1/1 HNO<sub>3</sub>/H<sub>2</sub>O (5 min), distilled water (5 min), acetone (5 min), and ethanol (5 min). In the furnace, they were first heated for about 1 h above the surface of the solution and then dipped into the solution for 5 min, at a temperature of 1 K above  $T_S$  so that the surface part of the substrate is dissolved and cannot introduce defects in the subsequent layer growth.

The epitaxial growth takes place for several hours at a temperature 1–6 K below the saturation temperature [19,49]. The 6 K difference corresponds to a supersaturation coefficient  $\sigma = 100(C_G/C_S - 1) \approx 5.3\%$  where  $C_G$  and  $C_S$  are the solute concentrations at the growth and saturation temperatures. All LPE growth experiments were performed with the crystal rotating at 40 rpm. After the epitaxial growth, the composite crystals were removed from the flux and cooled slowly to room temperature to prevent any thermal stress, which could produce cracks.

The dependence of the LPE growth velocity on the crystalline face was studied in [49]. It turns out that the epitaxial layer grows faster on the (010) face, Fig. 11a, which agrees with the fact that for bulk KLuW, the (010) face tends to be poorly developed, as mentioned above. The thickness of the epitaxial layer of KLu<sub>0.78</sub>Yb<sub>0.22</sub>W grown on a (010)-oriented KLuW substrate as a function of time is shown in Fig. 11b: For short growth times (about 6 h), the growth velocity is about 14.0  $\mu\text{m/h}$ .

The doping level for the epitaxial layers was 5–50 at. % for Yb [49] and 5 at. % for Tm [24]. Also for the epitaxial growth, the segregation coefficient of Yb and Tm was close to or larger than unity. It tends to decrease when the Yb concentration in the solution increases (Table 8). The *b*-orientation of the epitaxial layer was verified by X-ray diffraction [24]. There was no appreciable diffusion of the dopant from the layer into the substrate (Figs. 11a, 12).

The quality and the micromorphology of the grown epitaxial layers were studied by optical microscopy. Figure 13 shows a confocal image and profile schemes of the micromorphology observed in KLu<sub>0.5</sub>Yb<sub>0.5</sub>W/KLuW (010). As can be seen, no polygonalization of the growth steps occurs. The absence of polygonalization is due to

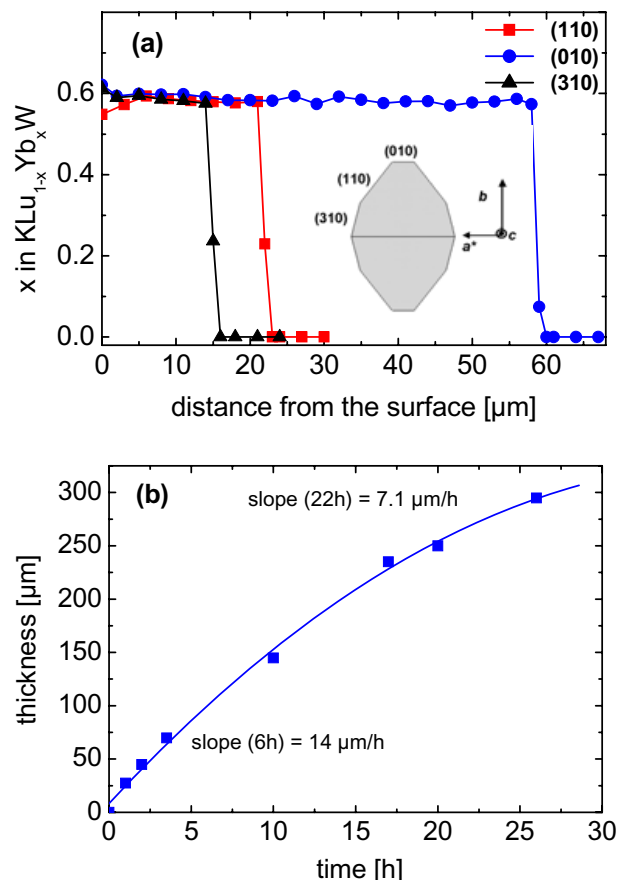


**Figure 11** Measured Yb-density profile for a Yb:KLuW/KLuW composite on three different faces (a) (the inset shows the faces studied), and growth velocity of a KLu<sub>0.78</sub>Yb<sub>0.22</sub>W epitaxial layer on the (010) face of a KLuW substrate (b).

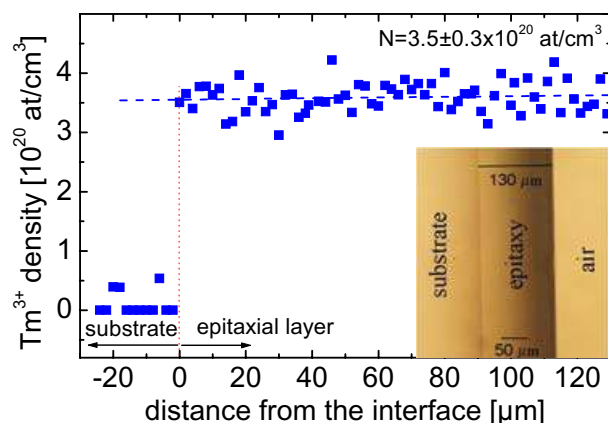


**Figure 12** Tm-density distribution for the (010) face of a Tm:KLuW/KLuW composite. The inset shows a microscope image of the layer region.

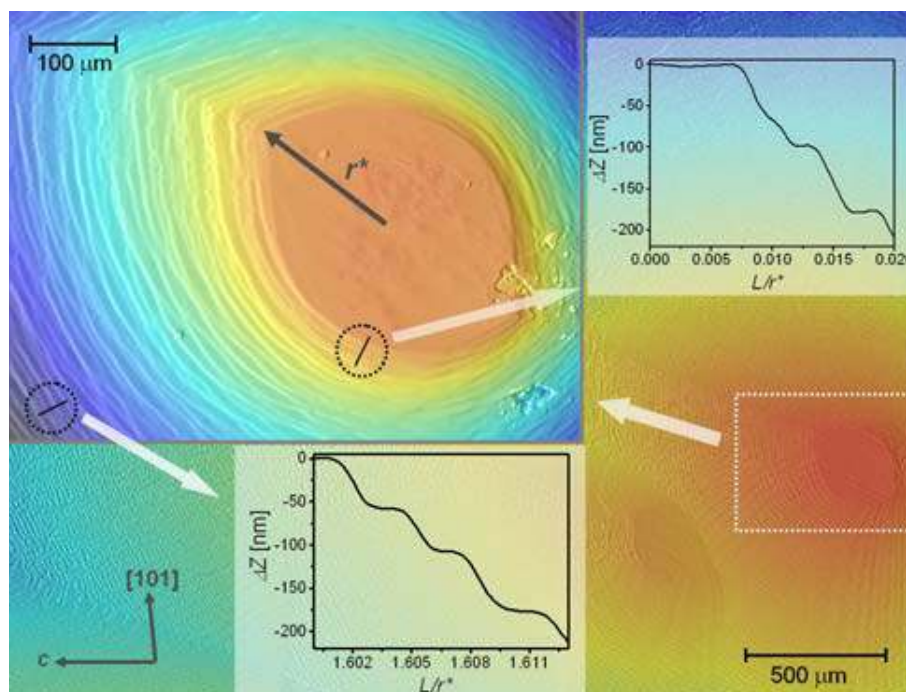


**Figure 13** Confocal image and scheme of the two screw dislocations of opposite sign leading to a complex hillock growth pattern, observed in KLu<sub>0.5</sub>Yb<sub>0.5</sub>W/KLuW (010). The graphs depict the height profile of the growth steps in two different regions of the growth micromorphology.

**Table 8** Segregation coefficient of Yb ( $K_{Yb}$ ) and chemical formula of the KLu<sub>1-x</sub>Yb<sub>x</sub>W film grown on KLuW, as functions of the Yb concentration in the solution.

Yb content in the solution [at. %]	$K_{Yb}$	chemical formula of the layer
5	1.24	KLu <sub>0.94</sub> Yb <sub>0.06</sub> W
10	1.23	KLu <sub>0.88</sub> Yb <sub>0.12</sub> W
20	1.11	KLu <sub>0.78</sub> Yb <sub>0.22</sub> W
50	1.04	KLu <sub>0.48</sub> Yb <sub>0.52</sub> W

the fact that the process is governed mainly by diffusion effects and not by structural effects related to the PBCs. The LPE growth is dominated by the superposition of two screw dislocations of opposite sign.

The distance between the growth steps amounts (in relative units normalized by the radius of the dislocations  $r^*$ ) to  $L/r^* \approx 0.0125$  for the step closest to the centre of the screw dislocations and increases with the separation from this centre. As can be seen from Fig. 13, the height of the growth steps strongly depends on the distance from the centre. It amounts to  $\approx 80 \mu\text{m}$  in the vicinity of the hillock centre but as the separation increases, the height of the growth steps decreases, e.g. to  $\approx 45 \mu\text{m}$  at  $L/r^* \approx 1.5$ . This effect is due to the splitting of the growth steps as seen in the marked area. Generally speaking, the epitaxial growth on the {010} faces exhibits mainly a flat surface, which indicates a layer-by-layer growth mechanism.

### 3. Properties of KLuW

The information previously available on the properties of KLuW was limited to the average refractive indices at  $0.7 \mu\text{m}$  ( $\approx 2.08$ ) [2] and  $0.9 \dots 1.4 \mu\text{m}$  ( $\approx 1.9$ ) [8], the transparency ( $0.3 \dots 5.5 \mu\text{m}$  for a thickness of 1 mm) [2,8], the average thermal conductivity ( $\approx 3 \text{ W/m/K}$ ) [2], and the hardness in the Moh's scale (4.5–5) [2]. We have collected in Table 9 the results obtained since the “re-discovery” of KLuW as a laser host in 2004, see also Table 1.

The transmission of KLuW is shown in Fig. 14. For this measurement a 1-mm thick *b*-cut plate was used [16]. At an absorption level of  $1 \text{ cm}^{-1}$  the transparency of KLuW extends from 365 to 5110 nm.

The monoclinic phase of KLuW belongs to the  $2/m$  point group. Hence, KLuW is a biaxial crystal with inversion centre. The three orthogonal principal optical axes  $x$ ,  $y$ ,  $z$  are traditionally labelled for monoclinic crystals as  $N_p$ ,  $N_m$ ,  $N_g$ . They are defined by the ratio of the corresponding refractive indices  $n_x < n_y < n_z$  or  $n_p < n_m < n_g$ . In monoclinic crystals one of the principal optical axes coincides with the 2-fold symmetry axis (the crystallographic *b*-axis). In the case of KLuW this is  $N_p$ . The other two principal optical axes lie in the *a*-*c* plane. We determined their orientation at 632.8 nm with two crossed Glan-Taylor polarizers.

Figure 15 shows the orientation of the optical ellipsoid with respect to the morphology and the crystallographic frame (both frames *abc* and  $N_p N_m N_g$  are right-handed). The principal optical axis  $N_g$  is located at  $18.5^\circ$  with

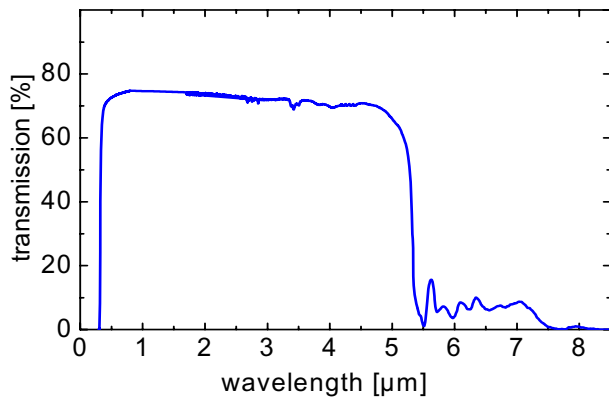


Figure 14 Unpolarized transmission of undoped KLuW.

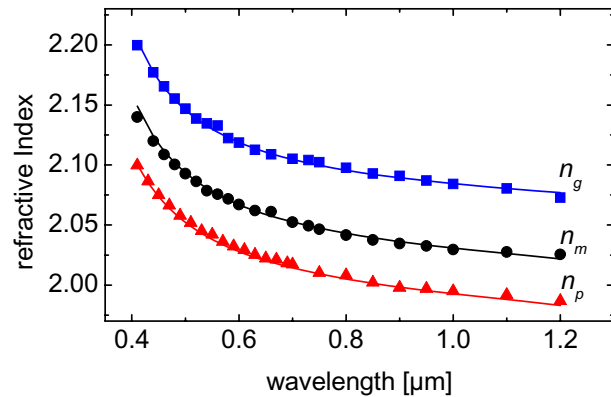


Figure 16 Dispersion of the refractive indices of undoped KLuW at room temperature.

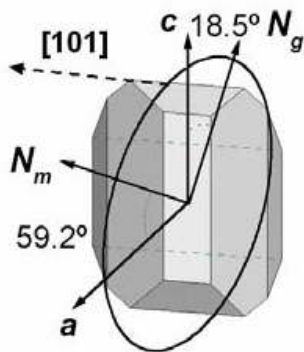


Figure 15 Optical ellipsoid of KLuW at room temperature.

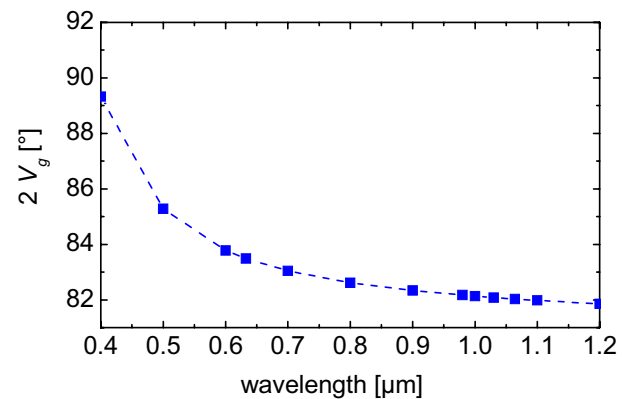


Figure 17 Angle between the two optic axes of KLuW.

respect to the  $c$  crystallographic axis and  $N_m$  is located at  $59.2^\circ$  with respect to the  $a$  crystallographic axis.

The dispersion curves for the three refractive indices were measured from 410 to 1200 nm by the minimum deviation method using semiprisms [30]. Two prisms cut in different principal planes were used and  $n_p$  was measured twice. The accuracy was  $5 \times 10^{-4}$ . Figure 16 shows the experimental values of the refractive indices and the fitted curves using Sellmeier equations containing a single UV pole and an IR correction term,  $n^2 = A + B/[1 - (C/\lambda)^2] - D\lambda^2$ . The obtained Sellmeier coefficients, valid in the visible and near-IR, are summarized in Table 10.

The angle  $2V_g$  between the two optic axes of KLuW is defined from  $\sin V_g = (n_g/n_m)(n_m^2 - n_p^2)^{1/2}(n_g^2 - n_p^2)^{-1/2}$ . Following the existing conventions, these axes are in the  $N_p$ - $N_g$  plane and the bisectrix of  $2V_g$  coincides with the  $N_g$  axis. Figure 17 shows the wavelength dependence of  $2V_g$  calculated from the measured refractive indices. In the whole wavelength range KLuW is an optically positive crystal ( $V_g < 45^\circ$ ).

In order to determine the linear expansion coefficients, the unit cell parameters of KLuW were measured as a function of the temperature by powder X-ray diffraction analysis, at temperatures of 298, 323, 373, 473, 573, 673 and 773 K [30]. This range of temperatures is sufficiently large to cover the variation of the unit cell parameters expected under conditions of laser operation. As can be seen from Fig. 18, the unit cell parameters  $a$ ,  $b$  and  $c$  increase and the angle  $\beta$  remains basically constant with temperature.

The linear thermal expansion coefficients in a given crystallographic direction are  $\alpha = (\Delta L/\Delta T)/L_{RT}$ , where  $L_{RT}$  is the initial parameter at 298 K (room temperature), and  $\Delta L$  is the modification of this parameter when the temperature is changed by  $\Delta T$ . The linear thermal expansion coefficients are obtained as slopes of the  $(\Delta L/L_{RT})$  dependence on the temperature  $T$  (Fig. 18). The values for monoclinic KLuW are  $\alpha_{100} = 10.6(2) \times 10^{-6}$ ,  $\alpha_{010} = 3.35(2) \times 10^{-6}$ ,  $\alpha_{001} = 16.3(2) \times 10^{-6}$ ,  $\alpha_{c*} = 15.1(1) \times 10^{-6}$ , and  $\alpha_V = 29.2(3) \times 10^{-6} \text{ K}^{-1}$ . From these results one can derive  $\alpha_{111}$  and, in this way, the

**Table 9** Some physical properties of the monoclinic KLuW crystal host. Data from [40] and [50] refer to 5 at. % Yb-doped KLuW.

properties	[Ref.]
temperature of polymorphic transformation/melting [K]	1312 <sup>+</sup> / 1326 <sup>+</sup> , 1330 [40]
crystal structure (space group – point group)	monoclinic centrosymmetric ( $C2/c \equiv C_{2h}^6 - 2/m$ ) [30]
site symmetry / coordination number / Lu <sup>3+</sup> ionic radius	$C_2 / 8 / 0.977 \text{ \AA}$ [30]
lattice constants	$a=10.576(7) \text{ \AA}$ , $b=10.214(7) \text{ \AA}$ , $c=7.487(2) \text{ \AA}$ , $\beta=130.68(4)^\circ$ , $Z=4$ [30]
cell volume and density	$613.3(6) \text{ \AA}^3$ and $7.686 \text{ g/cm}^3$ [30]
cation density / minimum Lu-Lu separation	$6.52 \times 10^{21} \text{ cm}^{-3} / 4.045(3) \text{ \AA}$ [30]
transparency range (1 cm <sup>-1</sup> level for 1 mm thickness)	365–5110 nm [20]
refractive index @ 1 $\mu\text{m}$	$n_p=1.995$ , $n_m=2.030$ , $n_g=2.084$ [30]
optical ellipsoid orientation (632.8 nm)	$N_p/b$ , $\angle(a, N_m)=59.2^\circ$ , $\angle(c, N_g)=18.5^\circ$ [30]
angle between the two optic axes at 1064 nm	$2V_g=82.03^\circ$ (optically positive) [30]
strongest phonon modes [cm <sup>-1</sup> ]	908 <sup>+</sup> , 756 <sup>+</sup> [3] <sup>f</sup>
specific heat @ 300 K / 363 K / 1099 K	324.4 <sup>+</sup> / 350 <sup>+</sup> (365) / (701) J/kgK ([40])
thermal conductivity coefficients $\kappa$ @ 298 K / 563 K	$\kappa_1=3.09/2.49 \text{ W/mK}$ , $\kappa_2=2.55/2.05 \text{ W/mK}$ , $\kappa_3=4.40/3.15 \text{ W/mK}$ [40]**
and orientation of the conductivity ellipsoid, $X_1X_2X_3$	$X_2/b$ , $\angle(a, X_1)=6.34^\circ/1.94^\circ$ , $\angle(X_3, c)=34.4^\circ/38.8^\circ$
thermal expansion coefficients $\alpha$ [ $10^{-6} \text{ K}^{-1}$ ] and	$\alpha_{11}=8.98(12.8)$ , $\alpha_{22}=3.35(7.8)$ , $\alpha_{33}=16.72(22.2)$ [30]*
orientation of the thermal expansion ellipsoid, $X_1X_2X_3$	$X_2/b$ , $\angle(a, X_1)=27.24^\circ(30.37^\circ)$ , $\angle(X_3, c)=13.44^\circ(10.37^\circ)$ ([50])**
microhardness numbers for planes $\perp$ (axis)	VH=440( <i>a</i> ), 410 ( <i>b</i> ), 560( <i>c</i> ) [30]
	VH=393.5 [11]***
	KHN=366 ( <i>a</i> ), 417 ( <i>b</i> ), 489 ( <i>c</i> ) [40]

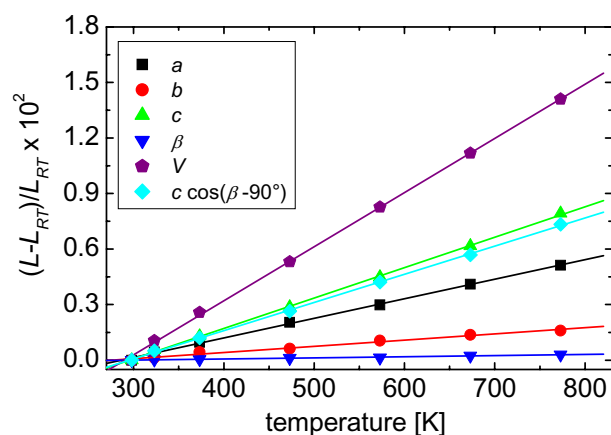
<sup>+</sup> unpublished (this work); <sup>f</sup> infrared and Raman spectra for 5 at. % Yb-doped KLuW can be found in [37];

\* measurements of the unit cell parameters at 298–773 K by powder X-ray diffraction;

\*\* measurements by a thermal dilatometer at 323–873 K [50], other data for 5 at. % Yb and 6 at. % Tm co-doped KLuW can be found in [29];

\*\*\* for 3 at. % Nd-doped KLuW with unspecified orientation.

References in additional brackets correspond to the values given in brackets.

**Figure 18** Evolution of the unit cell parameters of KLuW with temperature (RT: room temperature).

linear thermal expansion tensor at 298 K in a crystallo-physical coordinate system with orthogonal axes parallel to *a*, *b*, and *c*\*

By diagonalizing the obtained matrix one can obtain the linear thermal expansion tensor in the eigenframe *X*<sub>1</sub>,

**Table 10** Sellmeier coefficients of KLuW.

	<i>A</i>	<i>B</i>	<i>C</i> [ $\mu\text{m}$ ]	<i>D</i> [ $\mu\text{m}^{-2}$ ]
$n_p$	3.21749	0.75382	0.25066	0.05076
$n_m$	3.36989	0.74309	0.26193	0.04331
$n_g$	3.58334	0.73512	0.26700	0.02953

$X_2/b$ ,  $X_3$ . In monoclinic crystals the 2-fold symmetry axis (the crystallographic *b* axis) coincides with one of the principal axes. In the case of KLuW, this axis corresponds to the minimum thermal expansion coefficient, i.e.  $X_2$ . The diagonalized linear thermal expansion tensor has the following values:

$$\alpha_{ij} = \begin{pmatrix} 8.98 & 0 & 0 \\ 0 & 3.35 & 0 \\ 0 & 0 & 16.72 \end{pmatrix} \times 10^{-6} \text{ K}^{-1}$$

The principal axis with medium thermal expansion,  $X_1$ , is located at  $\rho = 27.24^\circ$  from the *a* axis and the principal axis with the maximum thermal expansion coefficient,  $X_3$ , is located at  $\delta = 13.44^\circ$  from the *c* axis. The thermal expansion ellipsoid is depicted in Fig. 19.

Comparing with previous data obtained for KGdW, KYW, KErW and KYbW [51], KLuW has a similar an-



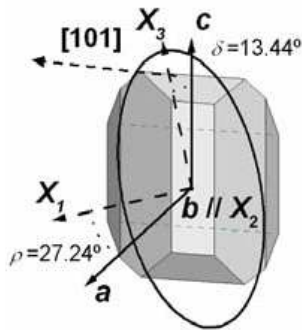


**Figure 19** Thermal expansion ellipsoid of KLuW.

gle between the  $X_3$  and the  $c$  axes. On the other hand, if the ratio  $\alpha_{33}/\alpha_{11}$  is considered as a measure of the linear thermal expansion anisotropy in the face  $\{010\}$  one can conclude that this anisotropy decreases along the KLuW series. Thus, KLuW is the host with the lowest thermal anisotropy in the  $\{010\}$  plane. This lowest anisotropy means reduced probability of cracking for thermal reasons when KLuW crystals are used as laser active elements. Finally, the calculated linear expansion coefficients along the principal optical axes  $N_p$ ,  $N_m$ , and  $N_g$ , amount to  $3.35 \times 10^{-6}$ ,  $11.19 \times 10^{-6}$ , and  $14.55 \times 10^{-6} \text{ K}^{-1}$ , respectively.

The specific heat of KLuW was measured by means of the relaxation method over a temperature range from the pumped helium temperature (2.5 K) up to about 400 K where it shows no anomaly, Fig. 20a. From the low temperature part of the data (phonon contribution), a Debye temperature of  $\theta_D \approx 303 \text{ K}$  was obtained, Fig. 20b.

Cutting and polishing are important prerequisites for successful applications of any crystal material. The techniques for cutting and polishing are directly related to the mechanical properties. High hardness values ensure better quality of the polished surfaces of the active elements.

Vickers static micro-indentations have been performed on three different faces of KLuW. The faces were cut and polished (to  $0.3 \mu\text{m}$  metallographic quality) perpendicular to the three crystallographic directions  $a^*$ ,  $b$  and  $c$ , respectively. The used strengths were 0.03, 0.05 and 0.1 N. The corresponding loading rates were 0.01, 0.02 and 0.05 N/s, respectively, and each indentation was for 1 s. For each load, different indentations were performed and the average diagonal imprints were used for the calculation. A scanning electron microscope was used to quantify the diagonal imprint of the residual indentation impression; the magnification was  $\times 12000$  [30].

The Vickers diamond pyramid hardness number ( $HV$ ) is defined by the applied load divided by the surface area of the indentation  $HV = \alpha_{HV} F/d^2$ , where  $F$  is the applied load in N,  $d$  is the arithmetic mean of the two diagonals,  $d_1$  and  $d_2$ . In Vickers hardness number (1 HV = 9.8 MPa), units  $\alpha_{HV} = 1.89 \times 10^5$ . Figure 21 shows a typical Vickers indentation on the (010) face of KLuW.

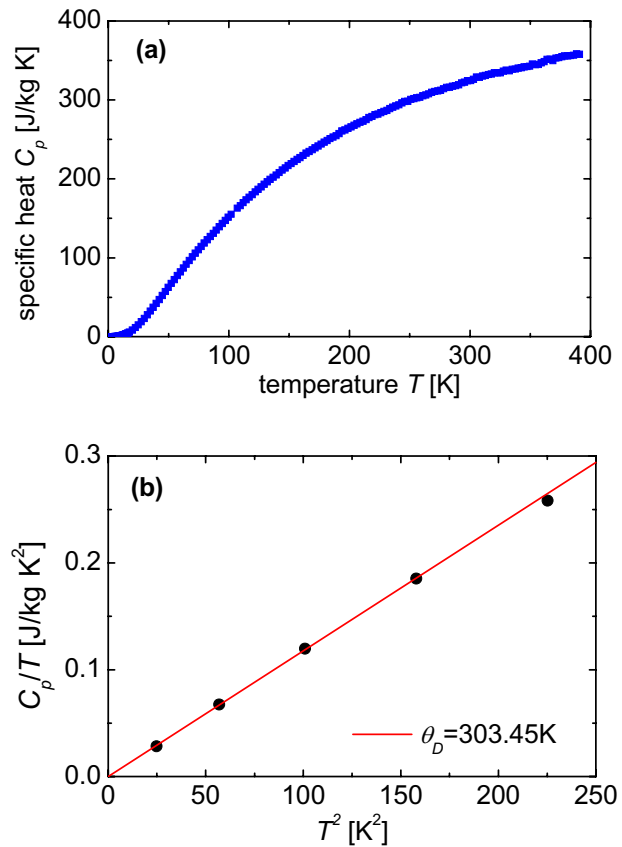


**Figure 20** Specific heat  $C_p$  of KLuW (a) and its lattice component  $C_p/T$  (b).

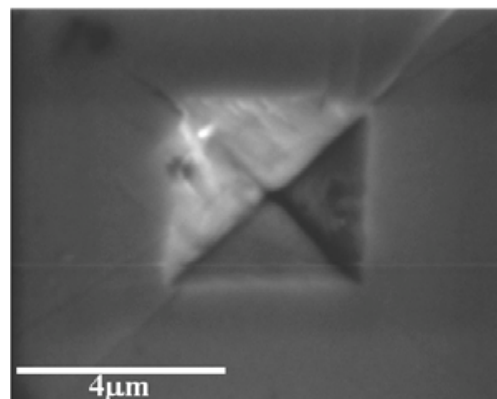


**Figure 21** Vickers indentation on the (010) face of KLuW with a load of 0.05 N.

The calculated  $HV$ , perpendicular to the  $a^*$ ,  $b$  and  $c$  directions of KLuW, is 440, 410 and 560 HV, respectively. Hence, this parameter exhibits pronounced anisotropy for KLuW. The Vickers value  $HV$  perpendicular to the  $b$  direction, transformed to the Moh's hardness scale, gives a value of about 4. Hence, the (010) face, being the softest, is not the proper choice from the point of view of efficient polishing procedure.

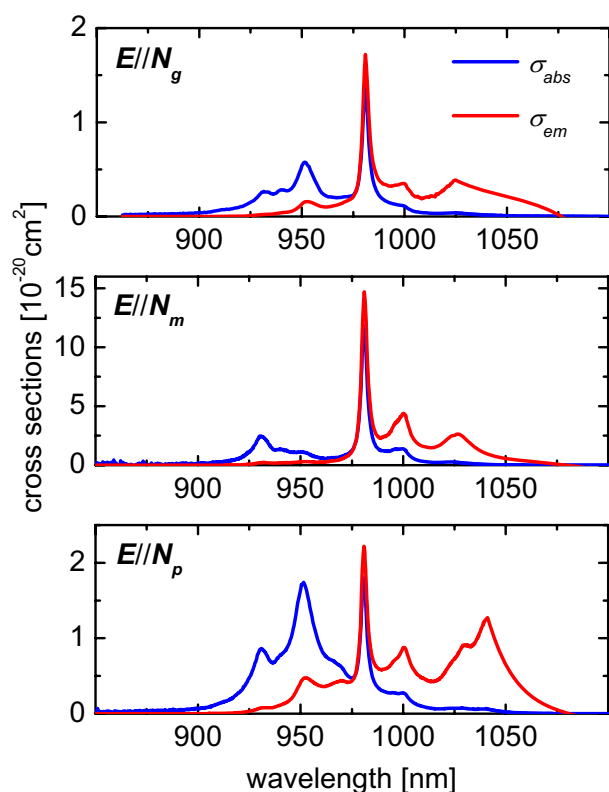


**Figure 22** Polarized measured absorption and calculated emission cross-sections of Yb:KLuW.

#### 4. Spectroscopy of Yb- and Tm-doped KLuW

Polarized optical absorption measurements of Yb:KLuW and Tm:KLuW at room temperature were performed in order to establish the best conditions for pumping of such lasers and to estimate the absorption and emission cross sections using the reciprocity method [52]. Here we focus only on the emission near 1  $\mu\text{m}$  and near 1.9  $\mu\text{m}$ , for the  $^2\text{F}_{5/2} \rightarrow ^2\text{F}_{7/2}$  and  $^3\text{F}_4 \rightarrow ^3\text{H}_6$  transitions of  $\text{Yb}^{3+}$  and  $\text{Tm}^{3+}$ , respectively, because these transitions were studied in the laser experiments (next sections). Polarized absorption and luminescence studies at low temperature (6–10 K) were used to determine the Stark levels of  $\text{Yb}^{3+}$  and  $\text{Tm}^{3+}$  in KLuW. The main spectroscopic parameters for the two dopants in bulk KLuW are summarized in Table 11.

$\text{Yb}^{3+}$  and  $\text{Tm}^{3+}$  have odd  $4f^{13}$  and even  $4f^{12}$  numbers of active 4f electrons, respectively. Both dopants, substituting  $\text{Lu}^{3+}$ , occupy a  $C_2$  symmetry site. The interaction with the crystal field results in splitting of the free ion  $2S+1L_J$  terms into  $(2J+1)/2$  Stark sublevels for  $\text{Yb}^{3+}$  and  $(2J+1)$  Stark sublevels for  $\text{Tm}^{3+}$ .

All samples used for spectroscopic characterization were cut and polished with their parallel faces normal to

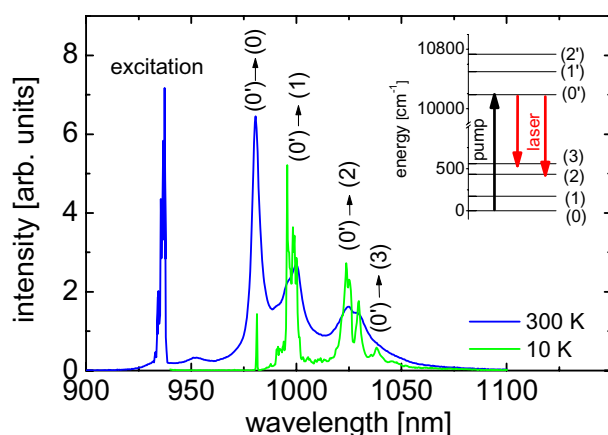


**Figure 23** Room temperature (blue line) and 10 K (green line) emission spectra recorded with 0.7 at. % Yb-doped KLuW. The inset shows the schematic diagram of the Stark levels and transitions of  $\text{Yb}^{3+}$  in KLuW.

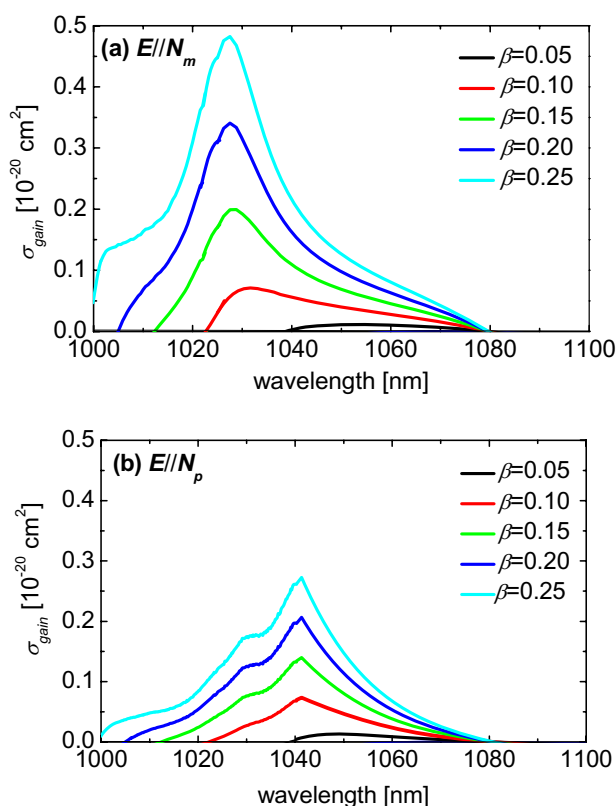


**Figure 24** Gain cross section  $\sigma_{\text{gain}} = \beta\sigma_{\text{em}} - (1 - \beta)\sigma_{\text{abs}}$  for polarization along the  $N_m$  (a) and  $N_p$  (b) axes of Yb:KLuW and different population inversion rates  $\beta$ .

one of the principal optical axes which allows to study the other two polarization directions.

**Table 11** Some spectroscopic properties of Yb- and Tm-doped monoclinic KLuW (from [15, 16, 22, 23, 33]).

spectral parameters	Yb:KLuW		Tm:KLuW	
segregation coefficient / maximum doping level	1.3-1.4 / 100%		1-1.2 / 20%	
lower laser level [cm <sup>-1</sup> ]	559	435	530	
thermal population @ 300 K [%]	4.22	7.64	1.94	
<sup>2</sup> F <sub>5/2</sub> fluorescence lifetime [μs]	275-299 (6.8 at. %) 254 (13 at. %)*		-	
calculated <sup>2</sup> F <sub>5/2</sub> radiative lifetime [μs]	320		-	
<sup>3</sup> F <sub>4</sub> fluorescence lifetime [ms]	-		1.34 (3.7 at. %), <sup>+</sup> 0.9 (5 at. %) <sup>+</sup>	
absorption wavelength for <i>E</i> // <i>N<sub>m</sub></i> and <i>E</i> // <i>N<sub>p</sub></i> [nm]	981.1	980.9	802	793.5
absorption linewidth for <i>E</i> // <i>N<sub>m</sub></i> and <i>E</i> // <i>N<sub>p</sub></i> [nm]	3.6	4	4	1
σ <sub>abs</sub> for <i>E</i> // <i>N<sub>m</sub></i> and <i>E</i> // <i>N<sub>p</sub></i> [10 <sup>-20</sup> cm <sup>2</sup> ]	11.8	1.8	5.95	9.96
laser (reference) wavelength λ <sub>ref</sub> [nm]	1040		1950	
emission bandwidth (FWHM) [nm]	≈22	≈28	-	-
σ <sub>em</sub> [10 <sup>-20</sup> cm <sup>2</sup> ] @ λ <sub>ref</sub>	1.01	1.24	1.20	0.57
σ <sub>reabs</sub> [10 <sup>-20</sup> cm <sup>2</sup> ] @ λ <sub>ref</sub>	0.06	0.07	0.11	0.025

\* pinhole method (this work), <sup>+</sup> pinhole method.**Table 12** Experimental Stark energy levels, *E*<sub>exp</sub>, of Yb<sup>3+</sup> and Tm<sup>3+</sup> ions observed in KLuW.

<sup>2</sup> S <sup>+</sup> <sub>1</sub> L <sub>J</sub>	<i>E</i> <sub>exp</sub> [cm <sup>-1</sup> ]
<sup>2</sup> F <sub>7/2</sub>	0, 175, 435, 559
<sup>2</sup> F <sub>5/2</sub>	10187, 10498, 10735

<sup>2</sup> S <sup>+</sup> <sub>1</sub> L <sub>J</sub>	<i>E</i> <sub>exp</sub> [cm <sup>-1</sup> ]
<sup>3</sup> H <sub>6</sub>	0, 135, 155, 224, 247, 256, 279, 329, 346, 359, 513, 522, 530
<sup>3</sup> F <sub>4</sub>	5663, 5711, 5724, 5768, 5876, 5963, 5976, 5981, 6002
<sup>3</sup> H <sub>5</sub>	8231, 8369, 8379, 8389, 8441, 8452, 8481, 8500, 8599, 8612, 8654
<sup>3</sup> H <sub>4</sub>	12603, 12606, 12717, 12729, 12744, 12790, 12801, 12883, 12906
<sup>3</sup> F <sub>3</sub>	14493, 14511, 14529, 14561, 14564, 14617, 14625
<sup>3</sup> F <sub>2</sub>	15078, 15081, 15103, 15123, --
<sup>1</sup> G <sub>4</sub>	21092, 21121, 21128, 21233, 21353, 21361, 21535, 21581, 21613
<sup>1</sup> D <sub>2</sub>	27743, 27808, 27987, 28000, 28050

Figure 22 shows the measured absorption and calculated emission cross sections for the single <sup>2</sup>F<sub>7/2</sub> ↔ <sup>2</sup>F<sub>5/2</sub> transition of Yb<sup>3+</sup> in KLuW and the three polarization directions. The maximum absorption cross-section at 981.1 nm calculated from the actual Yb<sup>3+</sup> concentration of 4.5 × 10<sup>19</sup> cm<sup>-3</sup> (0.7 at. % Yb-doped sample) amounts to 1.18 × 10<sup>-19</sup> cm<sup>2</sup> for *E*//*N<sub>m</sub>* (linewidth: 3.6 nm). Both values are very close to those reported for 5 at. % (in the solution) Yb-doped KYW or KGdW [53,54] and the stoichiometric KYbW (100 at. % Yb) [36]. The maximum absorption cross section for light polarization parallel to the *N<sub>m</sub>* principal optical axis is about 15 times larger than that of Yb:YAG [52]. The absorption profiles in Yb:KLuW, for all polarizations, are very suitable for pumping with InGaAs laser diodes operating near 980 nm. The maximum emission cross section in Yb:KLuW amounts to 1.47 × 10<sup>-19</sup> cm<sup>2</sup>, also for *E*//*N<sub>m</sub>* at 981.1 nm.

Similar to Yb:KYW and Yb:KGdW, the useful polarizations for Yb:KLuW are *E*//*N<sub>m</sub>* and *E*//*N<sub>p</sub>* because the emission cross sections for *E*//*N<sub>g</sub>* are very low. No differ-

ence was observed in the spectroscopy of thin Yb-doped epitaxial layers [49].

The energy position of the four sublevels of the ground state multiplet <sup>2</sup>F<sub>7/2</sub> and the three sublevels of the excited state multiplet <sup>2</sup>F<sub>5/2</sub> of Yb<sup>3+</sup> in KLuW obtained from low temperature absorption and emission spectroscopy are included in Table 12. The Stark splitting of the <sup>2</sup>F<sub>5/2</sub> multiplet is indicative of stronger crystal field in comparison to Yb:KYW and Yb:KGdW [53,54] which is advantageous for tunable and short pulse laser operation. Figure 23 shows emission spectra recorded at room and low temperature and the transitions involved in laser operation.

In the quasi-three-level laser system of Yb<sup>3+</sup> the potential gain bandwidth for tunable or mode-locked operation can be estimated by calculating the gain cross section which depends on the inversion rate. This is illustrated in Fig. 24 for the two polarizations *E*//*N<sub>m</sub>* and *E*//*N<sub>p</sub>*.

Measurements of the fluorescence lifetime performed with a low doped, 0.7 at. % Yb:KLuW, sample to minimize the effect of radiation trapping yielded a decay curve

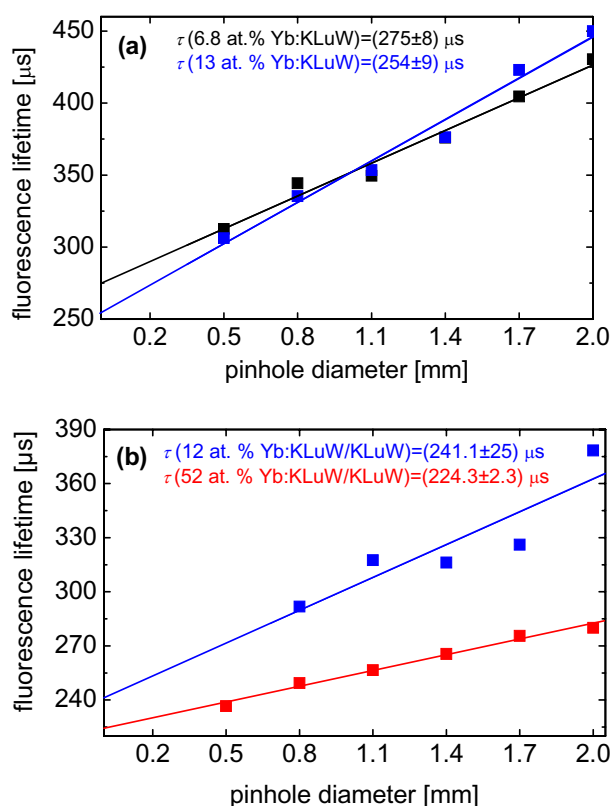


**Figure 25** Fluorescence lifetime measurements using the pinhole method of bulk (a) and epitaxial (b) Yb:KLuW.

that could be fitted by a single exponential corresponding to a time constant of 375 μs [16]. The use of the pinhole method [55] which allows to eliminate this effect at higher doping gave for different samples of 6.8 at. % Yb-doped KLuW values of 299 and 275 μs. Figure 25 shows the results of simultaneous measurements of two bulk and two (010) epitaxial samples which demonstrate the weak quenching effect in this material. Using the same procedure as in [36], i.e. the Füchtbauer-Ladenburg equation, an estimation of 320 μs was obtained for the radiative lifetime of Yb:KLuW by averaging over the emission spectra for the three polarizations. More data on the spectroscopy of Yb:KLuW can be found in [16].

The polarized room temperature absorption spectra of Tm<sup>3+</sup> in KLuW were measured with a sample of 3.7 at. % Tm-doping (Tm<sup>3+</sup> density of  $2.41 \times 10^{20}$  cm<sup>-3</sup>). Figure 26 shows the absorption cross sections for the <sup>3</sup>H<sub>6</sub> → <sup>3</sup>H<sub>4</sub> transition, and the measured absorption and calculated, by the reciprocity method, emission cross sections for the <sup>3</sup>H<sub>6</sub> ↔ <sup>3</sup>F<sub>4</sub> transition of Tm<sup>3+</sup> in KLuW. Strong anisotropy is characteristic for the KLuW host and this is manifested also in the case of Tm-doping.

Similar to the case of Yb-doping, the useful polarizations for Tm:KLuW are  $E//N_m$  and  $E//N_p$  because the cross sections for  $E//N_g$  are very low. The maxi-

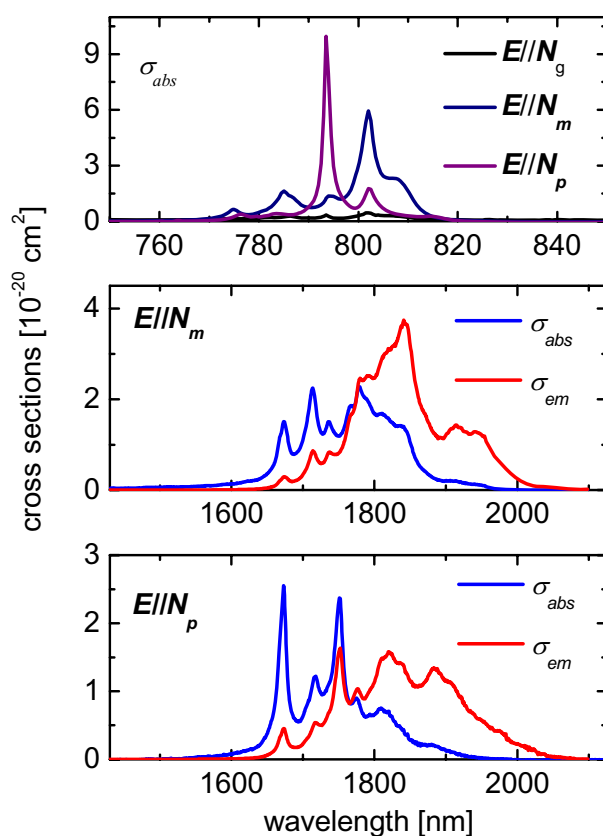


**Figure 26** Polarized absorption cross sections of Tm:KLuW for the <sup>3</sup>H<sub>6</sub> → <sup>3</sup>H<sub>4</sub> transition, and absorption and emission cross sections of Tm:KLuW for the <sup>3</sup>H<sub>6</sub> ↔ <sup>3</sup>F<sub>4</sub> transition and polarizations  $E//N_m$  and  $E//N_p$ .

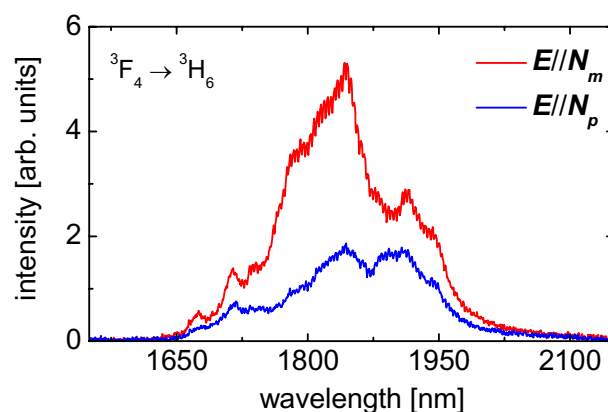


**Figure 27** Room temperature polarized emission spectra for the 1.9 μm transition of Tm<sup>3+</sup> in KLuW recorded with a 3.7 at. % Tm-doped sample.



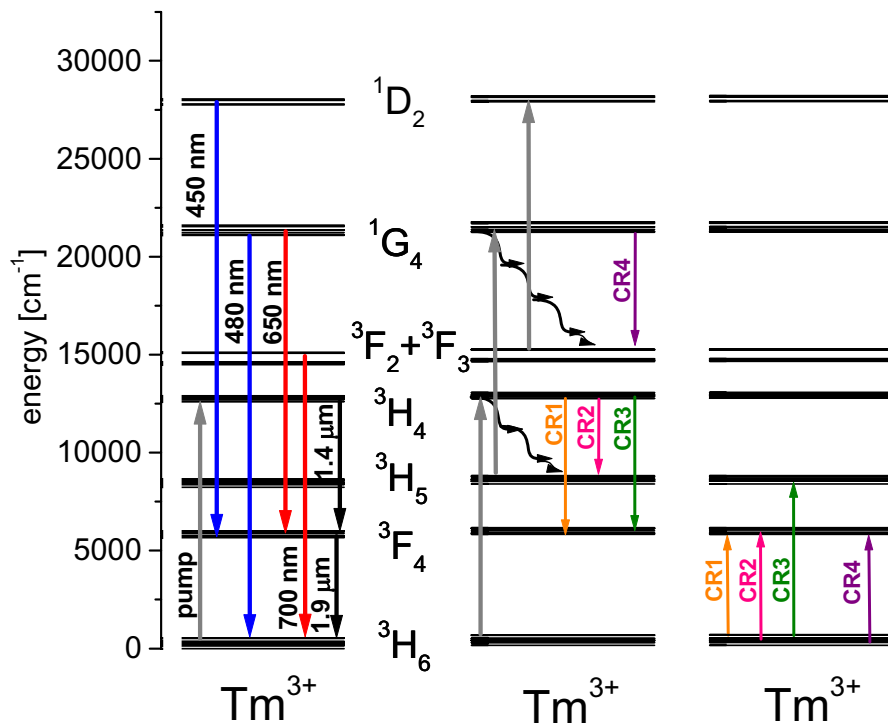


**Figure 28** Energy diagram of  $\text{Tm}^{3+}$  in KLuW with arrows indicating radiative and non-radiative processes; CR: cross relaxation.

imum absorption cross section for the  $^3\text{H}_6 \rightarrow ^3\text{H}_4$  transition amounts to  $5.95 \times 10^{-20} \text{ cm}^2$  for  $E//N_m$  at 802 nm. This main line with a width of 4 nm is very suitable for diode pumping with AlGaAs laser diodes emitting near 800 nm. The maximum absorption cross section for  $E//N_p$  amounts to  $9.96 \times 10^{-20} \text{ cm}^2$  at 793.5 nm but this Stark component has a width of only 1 nm. The above values are similar to those known for Tm-doped KGdW [56], KYW [57], and KYbW [58].

The maximum emission cross section for the  $^3\text{F}_4 \rightarrow ^3\text{H}_6$  transition amounts to  $3.71 \times 10^{-20} \text{ cm}^2$  for  $E//N_m$  at 1841 nm. For polarization  $E//N_p$ , the maximum emission cross section is  $1.58 \times 10^{-20} \text{ cm}^2$  at 1820 nm. Room temperature luminescence spectra for this transition were recorded under 802 nm excitation, Fig. 27. Using the experimentally measured luminescence profiles and the radiative lifetime calculated by the Judd-Ofelt method, the emission cross sections were calculated in [33] also using the Füchtbauer-Ladenburg equation: for  $E//N_p$  they were similar in magnitude to the results in Fig. 26 but for  $E//N_m$  – roughly 2 times lower.

The energy levels of  $\text{Tm}^{3+}$  in KLuW (Stark sublevels) were determined from low-temperature (6 K) absorption and emission spectroscopy using a sample of 0.6 at. % doping [33]. The results are included in Table 12. The upper level  $^3\text{F}_4$  for the 1.9  $\mu\text{m}$  transition can be populated by non-radiative relaxation and by four cross relaxation processes, as shown in Fig. 28.

The Stark splitting of a given manifold in Tm:KLuW is stronger than in Tm:KGdW. This again indicates stronger

crystal field in KLuW. In particular, the larger splitting of the ground state is favourable because this leads to less thermal population of the lower level in quasi-four-level laser operation. Further spectroscopic information on the other transitions can be found in [33].

Thulium lasers operate for the 1.9  $\mu\text{m}$  transition as a quasi-four-level system and their spectral characteristics can be predicted from the corresponding gain cross sections (Fig. 29). Somewhat higher gain is predicted for the  $E//N_m$  polarization while for the  $E//N_p$  polarization the lower wavelength limit seems slightly extended. Also, at lower inversion levels there is a trend that the supported gain bandwidth is larger for the  $E//N_p$  polarization.

In general the fluorescence lifetime values for the  $^3\text{F}_4$  level, obtained using the pinhole method, are shorter than previous measurements of Tm:KYW and Tm:KGdW without taking into account the reabsorption effect. However, using the same method, the lifetimes measured in KLuW and KGdW were equal [23]. There is some dependence of the fluorescence lifetime of Tm:KLuW on the doping level (quenching): 1.34 ms and 0.9 ms were obtained using samples of 3.7 and 5 at. % doping, Fig. 30 (see Table 4). The radiative lifetime calculated using the Judd-Ofelt method amounts to 1.483 ms [33].

## 5. Bulk and epitaxial Yb:KLuW lasers

The laser operation of the bulk and epitaxial Yb:KLuW samples was studied in three- or four-mirror cavities

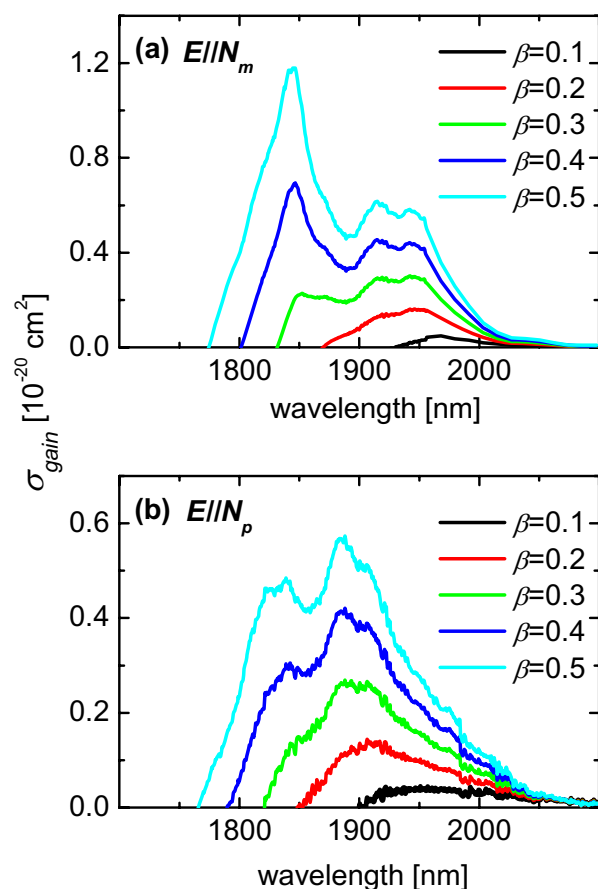


**Figure 29** Gain cross section  $\sigma_{gain} = \beta\sigma_{em} - (1-\beta)\sigma_{abs}$  for polarization along the  $N_m$  (a) and  $N_p$  (b) axes of Tm:KLuW and different population inversion rates  $\beta$ .

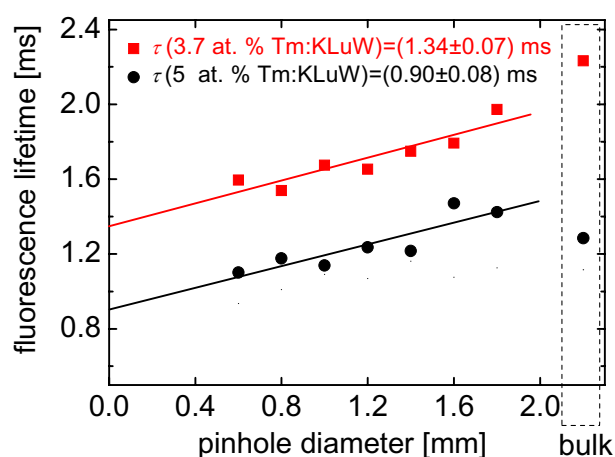


**Figure 30** Dependence of the measured lifetime of the  $^3F_4$  level of Tm<sup>3+</sup> in KLuW on the pinhole diameter for 3.7 and 5 at. % doping levels. Bulk: no pinhole.

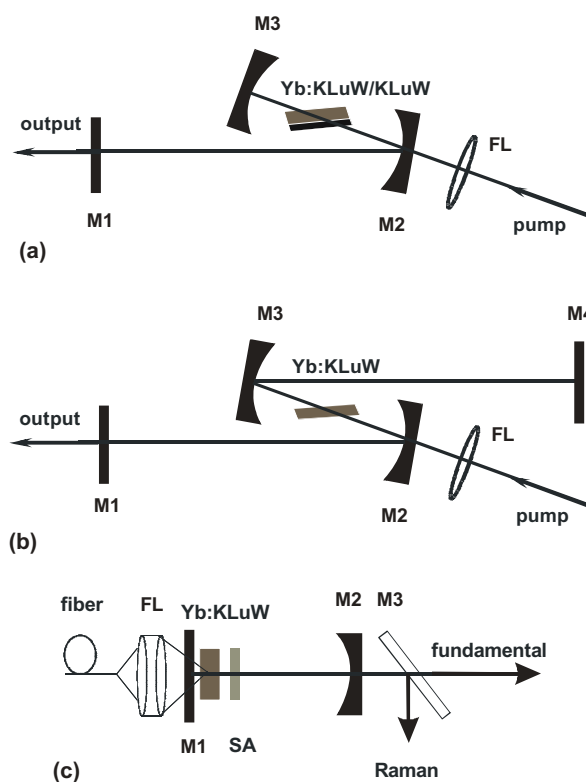


**Figure 31** Astigmatically compensated three- (a) and four- (b) mirror cavities for longitudinal pumping of the Yb:KLuW laser. In (a), the radii of curvatures, RC, of M3 and M2 are  $-5$  and  $-10$  cm, respectively; in (b) the folding mirrors (M2-M3) have RC =  $-10$  cm; in both cases FL is a lens with  $f = 6.28$  cm. Hemispherical cavity for power scaling (c): The output coupler (M2) has a RC =  $-2.5$  cm, SA denotes saturable absorber, and M3 is a dichroic mirror separating the fundamental and Raman radiation.

(Figs. 31a,b) with Ti:sapphire laser (1 nm linewidth) pumping or using a tapered diode laser (TDL) with 1 nm linewidth and  $M^2 < 3$  for the slow axis. The uncoated crystals were positioned under Brewster angle which determines the laser polarization and the pump polarization was always in the same plane. A simple two-mirror cavity (Fig. 31c) was used for power scaling, pumping by an unpolarized fiber coupled diode module (116  $\mu$ m core diameter, 0.2 NA) with  $f = 6.2$  mm micro-optics.

CW laser operation was studied first by placing the bulk crystals of Yb:KLuW between the two focusing mirrors of the Z-type cavity from Fig. 31b. With Ti:sapphire laser pumping and without special cooling, the CW laser performance of a 6.8 at. % Yb:KLuW (2.8 mm thick) sample and a 13 at. % Yb:KLuW (2.2 mm thick) sample, both with  $b(N_p)$ -cut, was very similar in terms of efficiency against absorbed pump power  $P_{abs}$ , Figs. 32a,b and Table 13. There was only slight difference in the optimum pump ( $\lambda_P$ ) and the oscillation ( $\lambda_L$ ) wavelengths. This is

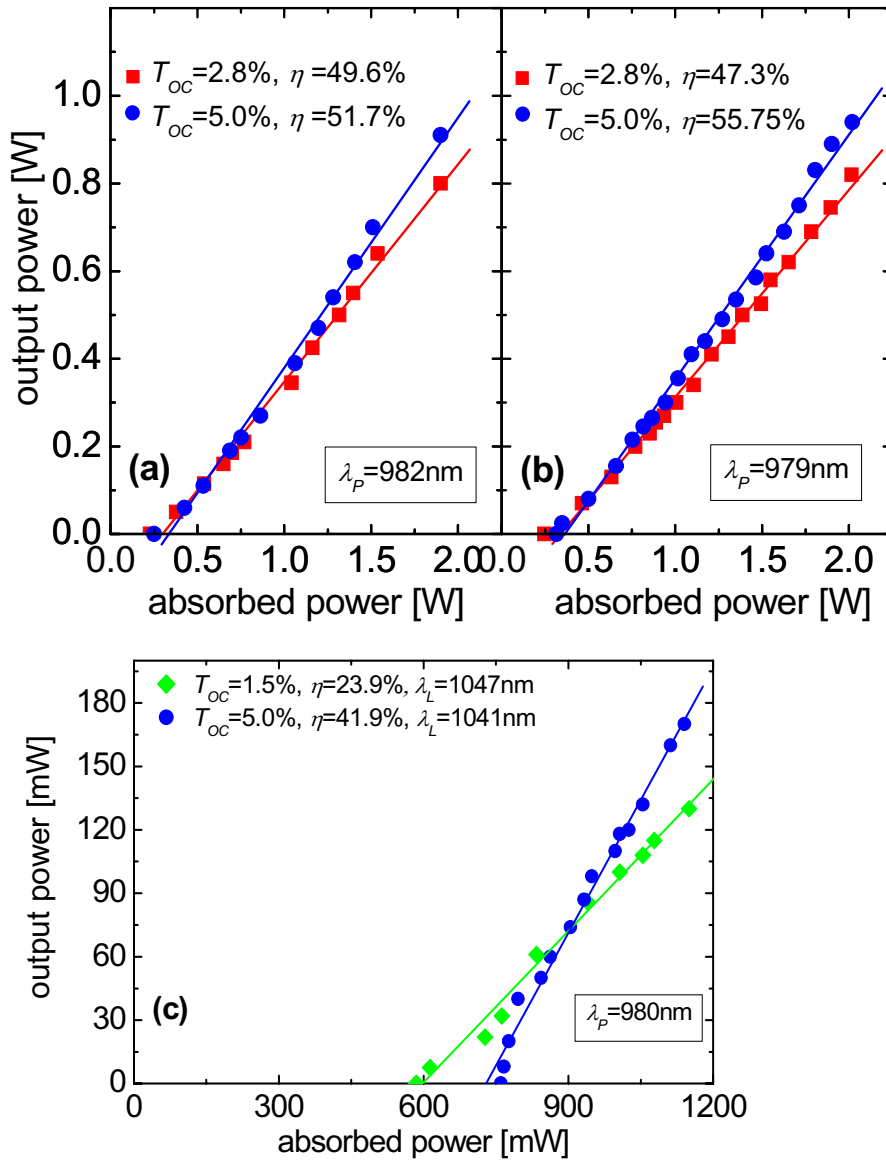


**Figure 32** Output power versus absorbed pump power of the Ti:sapphire laser pumped Yb:KLuW laser using the 140-cm long cavity from Fig. 31b with double pass pumping (through 80% retroreflection of the residual pump by the cavity mirrors) for two different output couplers  $T_{OC}$ : 6.8 at. % Yb-doping (a) and 13 at. % Yb-doping (b). Input-output characteristics obtained with single pass TDL pumping of the same 6.8 at. % Yb:KLuW sample in the same cavity from Fig. 31b (c). In all cases the pump and laser polarizations are  $E//N_m$ .

an indication of the unaffected crystal quality and upper level lifetime by the increased doping. With an output coupler of transmission  $T_{OC} = 2.8\%$ , the Yb:KLuW laser threshold could be reached for  $965 \text{ nm} < \lambda_P < 1005 \text{ nm}$ . The optimum Ti:sapphire laser pump wavelength for the 6.8 at. % Yb-doped KLuW sample was  $\lambda_P = 982 \text{ nm}$  and for the 13 at. % Yb-doped KLuW sample it was  $\lambda_P = 979 \text{ nm}$ . On the basis of the absorption spectrum in Fig. 22 the necessity to pump below the main absorption maximum in the case of higher doping can be explained by the lower absorption there which allows more homogeneous pumping along the sample thickness with reduced reabsorption. In both samples, for a pump beam waist of the order of  $30 \mu\text{m}$  we observed bleaching of the absorption

at the pump wavelength  $\lambda_P$ : At maximum pump powers, 450–480 mW and 520–550 mW were transmitted behind the 6.8 at. % and the 13 at. % Yb-doped KLuW samples, respectively, while near the threshold the whole incident pump power was absorbed in the first pass. The maximum output power for both crystals was  $P_{\text{out}} \approx 1 \text{ W}$  ( $T_{OC} = 5\%$ ) for an absorbed power of  $\approx 2 \text{ W}$ . The maximum output powers  $P_{\text{out}}$  and the optical-to-optical efficiency with respect to the absorbed power  $\eta_0$  are summarized in Table 13. The longer oscillation wavelengths  $\lambda_L$  with the higher Yb-doped KLuW are a consequence of the increased reabsorption. Since the saturated gain always equals the total losses, the decreasing  $\lambda_L$  when increasing  $T_{OC}$  can be

**Table 13** Maximum output power  $P_{\text{out}}$  and optical-to-optical efficiency  $\eta_0$  achieved with bulk Yb:KLuW.

6.8 at. % Yb:KLuW $P_{\text{abs}}=1.90$ W, $\lambda_p=982$ nm				13 at. % Yb:KLuW $P_{\text{abs}}=2.02$ W, $\lambda_p=979$ nm		
$T_{\text{OC}}$ [%]	$P_{\text{out}}$ [mW]	$\eta_0$ [%]	$\lambda_L$ [nm]	$P_{\text{out}}$ [mW]	$\eta_0$ [%]	$\lambda_L$ [nm]
1.5	465	24.5	1047.2	490	24.3	1051.3
2.8	800	42.1	1043.6	820	40.6	1049.0
5	910	47.9	1041.2	940	46.5	1046.5
10	965	50.8	1033.3	1010	50.0	1041.0

also attributed to the wavelength dependent reabsorption losses, see Fig. 24.

The imperfect overlap of the laser and pump modes in the case of TDL pumping resulted in increased thresholds and reduced slope efficiency  $\eta$ : At the optimum pump wavelength of  $\lambda_p = 980$  nm the recorded output power versus absorbed power is shown in Fig. 32c. The maximum  $P_{\text{out}} = 170$  mW ( $T_{\text{OC}} = 5\%$ ) for  $P_{\text{abs}} = 1.14$  W gives an optical-to-optical efficiency of  $\eta_0 = 15\%$ . The bleaching of the absorption in the case of Ti:sapphire laser pumping was suppressed when the laser was aligned as a result of the increased pump saturation intensity in the quasi-three-level Yb-system. In contrast, no bleaching was observed in the case of TDL pumping. The almost unchanged oscillation wavelengths  $\lambda_L$  in Fig. 32c in comparison to Figs. 32a,b and Table 13 indicate, however, that the net gain should be almost the same.

The  $E//N_p$  polarization was studied with an analogous 6.8 at. % Yb-doped KLuW (3 mm thick) sample with  $N_m$ -cut. For an absorbed power of 1.7 W (Ti:sapphire laser pumping), an output power of  $P_{\text{out}} = 750$  mW was obtained at 1046 nm using an output coupler with  $T_{\text{OC}} = 5\%$  ( $\eta = 54.2\%$ ) which is close to the 800 mW obtained for  $E//N_m$  with the 5 at. % Yb-doped  $b$ -cut sample (Fig. 32a). The thresholds with these two samples for  $T_{\text{OC}} = 5\%$  were 280 and 250 mW, respectively.

Power scaling in the CW regime was studied using a 3-mm thick, uncoated KLuW sample with 5.24 at. % Yb-doping and  $b$ -cut, mounted in a water-cooled Cu-block, and placed in the compact plano-concave cavity depicted in Fig. 31c, as close as possible ( $\approx 0.2$  mm) to the plane mirror M1. The pump waist in the position of the crystal was 40  $\mu\text{m}$ . The laser was optimized by adjusting the cavity length, operating near the hemispherical configuration. The oscillation wavelength was dependent on the output coupling, decreasing from  $\lambda_L = 1052.4$  nm for  $T_{\text{OC}} = 2\%$  to  $\lambda_L = 1039.5$  nm for  $T_{\text{OC}} = 10\%$ . The output beam was linearly polarized with  $E//N_m$  independent of the output coupling.

Figure 33a shows the input-output characteristics for  $T_{\text{OC}} = 2\%$ , 5%, and 10%; output couplings of 0.5–2% led to very similar results. The laser configuration used precluded any measurement of the absorbed pump power

under lasing conditions because of the strongly divergent nature of the pump beam. Therefore, the output power is plotted in Fig. 33a against the pump power incident on the crystal. The absorbed power at threshold can be determined because the small-signal absorption remains unchanged at low intracavity laser intensity. The absorbed pump power for reaching the laser threshold was 0.39, 0.57, and 0.81 W, for  $T_{\text{OC}} = 2\%$ , 5%, and 10%, respectively.

The most efficient operation was realized applying the  $T_{\text{OC}} = 2\%$  output coupler. At an incident pump power of 6.8 W, the output power reached 3.28 W leading to an optical-to-optical efficiency of  $\eta_0 = 48.2\%$ ; the slope efficiency at high pump powers exceeding 4.0 W was  $\eta = 78.2\%$ . By moving the crystal away from the pump focus, the small-signal absorption for the pump light was estimated to be 85%–90%. Assuming that under lasing conditions the bleaching effect would be balanced by the increase in the absorption due to the intracavity intensity, it is clear that the slope efficiency obtained with respect to the absorbed pump power is very close to the quantum-defect limit of 93%. For  $T_{\text{OC}} = 5\%$  and 10%, the highest output power obtained was  $P_{\text{out}} = 2.78$  W and 2.61 W, corresponding to slope efficiencies of  $\eta = 73.0\%$  and 71.8%, respectively. The absence of an output power roll-off in Fig. 33a at the highest pump level applied indicates a potential for further power scaling. The deviation of the input-output characteristics from the linear law in Fig. 33a, i.e. the lower efficiency in the pump power range below 4.0 W, is attributed mainly to the lower absorption (0.55–0.57 as compared to 0.6–0.72 for pump powers above 4.5 W, measured without lasing). This pump absorption variation is caused by the wavelength shift of the diode laser which emitted a multi-peaked spectrum: Its centre wavelength changed from 973 to 978 nm with increasing output power.

By introducing a Cr<sup>4+</sup>:YAG saturable absorber (a 1 mm thick AR-coated plate with 80% transmission) into the cavity (Fig. 31c), passively Q-switched laser operation was achieved. Since SRS was expected to occur in the nanosecond regime, the incoupling mirror M1 was chosen highly reflecting both at the laser and Raman wavelengths. To stabilize the laser, the physical cavity length was shortened from 25 to 22 mm, and in order to avoid multi-pulse operation, a sufficiently large output coupling was required. The most appropriate output coupler available for this experiment had a transmission of 10% at 1030 nm and about 20% near the Raman line at 1140 nm. Slightly above the threshold (4.28 W of incident pump power), SRS occurred and the output spectrum consisted of the fundamental line at 1030.6 nm and the 1<sup>st</sup> Stokes line at 1137.6 nm which obviously corresponds to the Raman-active vibration mode  $\nu_1$ , see Table 2. Figure 33b shows the input-output characteristics of the passively Q-switched Yb:KLuW laser with simultaneous SRS self-conversion. At the highest available pump power (7 W incident on the Yb:KLuW crystal), the total average output power reached 1.3 W. The part of the Raman radiation



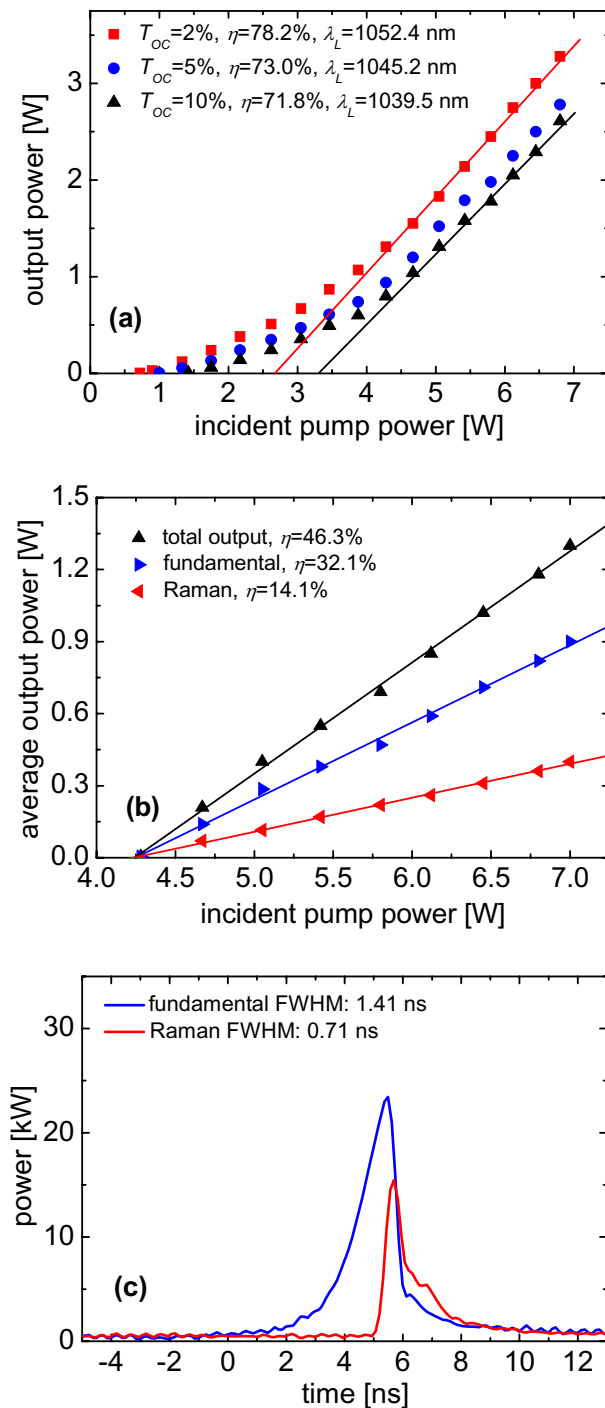


**Figure 33** Output power versus absorbed pump power of the CW Yb:KLuW laser pumped by an unpolarized fiber-coupled diode in the 2.5 cm long plano-concave cavity from Fig. 31c (a), average powers in the Q-switched regime (b), and temporal pulse profiles recorded at a repetition rate of 28 kHz (c).

was 0.4 W. The optical-to-optical efficiencies with respect to the incident pump power were  $\eta_0 = 18.6\%$ ,  $5.7\%$ , and  $12.9\%$ , for the total, the Raman, and the fundamental radiation, respectively. The corresponding slope efficiencies were  $\eta = 46.3\%$ ,  $14.1\%$ , and  $32.1\%$ . It can be seen from Fig. 33b that, as in the case of CW operation, no roll-off occurred up to the highest pump level applied, suggesting that the laser can be further power scaled. The linear dependence of the output characteristics in Fig. 33b is due to the high Q-switching threshold. This is consistent with the CW operation results at higher pump powers.

For a passively Q-switched laser, the pulse repetition frequency depends on the pump power. In the present laser it increased almost linearly from 6 kHz at threshold to 28 kHz at the highest pump level. The maximum energies of the fundamental and Raman pulses at 28 kHz were 32.4 and 14.4  $\mu\text{J}$ , respectively.

The temporal pulse profiles (see Fig. 33c) indicate pulse durations (FWHM) of 1.41 ns for the fundamental and 0.71 ns for the Raman radiation. The pulse-to-pulse fluctuations for both the fundamental and the Raman radiation were estimated to be less than 5%. A peak power of 23 kW for the fundamental pulse was calculated from the values of the pulse energy and the duration. For accurate estimation of the peak power of the Raman pulse we took into account its exact temporal shape (Fig. 33c) and arrived at 15.2 kW.

In comparison to previous work on Q-switching performed with Yb:KYW and Yb:KGdW, the laser performance of Yb:KLuW is superior with respect to the pulse energy, duration, and peak power [59–61]. In terms of energy and peak power the results are higher by more than one order of magnitude than those reported in [59] and [60], and although comparable pulse durations were given in [61], the improvement in terms of energy and peak power is still at least 3–4 times and 2 times, respectively. The efficiencies achieved with Yb:KLuW are also higher.

The CW laser experiments with an uncoated 12 at. % Yb:KLuW epitaxial sample (a 100  $\mu\text{m}$  layer grown on a 1.1 mm thick undoped substrate) were performed in the V-type cavity shown in Fig. 31a without special cooling. Again, the 1.2 mm thick *b*-cut Yb:KLuW/KLuW(010) crystal was placed under Brewster angle between the two focusing mirrors. The sample was oriented for propagation along the *b*( $N_p$ ) axis with faces parallel to the  $N_m$ - $N_g$  plane and polarization along the  $N_m$  principal optical axis. The CW input-output characteristics are presented in Fig. 34a. We limited the incident pump power applied to 1.85 W. The maximum output power of  $P_{\text{out}} = 415$  mW measured corresponds to an optical-to-optical efficiency of  $\eta_0 = 55\%$  with respect to the absorbed pump power ( $T_{OC} = 3\%$ ). The slope efficiency with respect to the absorbed power increases with  $T_{OC}$  reaching a maximum value of  $\eta = 66\%$  ( $T_{OC} = 10\%$ , Fig. 34a). The efficiencies exceed those achieved with the 2.2-mm thick 13 at. % Yb-doped bulk KLuW in the similar pump and laser configuration from Fig. 31b. This is attributed to the strongly reduced

reabsorption which leads to about 4 times lower thresholds in the case of the epitaxial sample (about 70 mW in Fig. 34a) and to shorter laser wavelengths  $\lambda_L$ . The relatively short oscillation wavelength  $\lambda_L$  (Fig. 34a) can be also attributed to the stronger bleaching of the absorption (Fig. 35).

The dependence of the actual absorption (the low-signal absorption of this epitaxy was about 64%) on the output coupling is also rather pronounced (Fig. 35), just as a consequence of the strong absorption bleaching when lasing is interrupted. In the case of Ti:sapphire laser pumping the absorption is bleached at relatively low incident powers (in this range it cannot be reliably estimated) and the further dependence on the incident pump power is rather weak.

We examined the influence of thermal effects by employing a chopper with a 1:10 duty cycle. We observed only a weak effect of about 10% at the maximum applied pump powers (see Fig. 34a), i.e. the maximum average output power achieved with the chopper was 45 mW.

Recycling of the pump using another end mirror M3 in Fig. 31a, it was possible to increase the output power in the CW regime to  $P_{\text{out}} = 515$  mW ( $T_{OC} = 3\%$ ) at  $\lambda_L = 1030$  nm as a result of the increased absorption in the two pump passes [19]. It is interesting to note that even without cooling no damage of the epitaxial crystal occurred regardless of the high power levels (intracavity intensity exceeding 1 MW/cm<sup>2</sup> with the  $T_{OC} = 1.1\%$  output coupler) in the case of double pass pumping.

Using the TDL for single pass pumping in the same set-up, CW laser operation was obtained for output coupler transmission between 1.1% and 10%, Fig. 34b. Also in this case, the laser thresholds obtained were lower (3 to 5 times) in comparison to the bulk Yb:KLuW sample, e.g. as low as  $P_{\text{abs}} \approx 120$  mW for  $T_{OC} = 1.1\%$ . This might be related to the improved overlap of the pump and laser modes in the thin epitaxial layer. At the maximum applied pump power (1.25 W incident on the sample) the maximum output power amounted to  $P_{\text{out}} = 105$  mW and the optical-to-optical efficiency with respect to the absorbed power reached  $\eta_0 = 20\%$  ( $T_{OC} = 3\%$ ). The highest slope efficiency with respect to the absorbed power,  $\eta = 37.1\%$ , was achieved with the  $T_{OC} = 5\%$  output coupler, Fig. 34b.

The actual absorption depends on the bleaching effect and, as already mentioned, can be substantially lower than the small-signal value. It depends, however, also on the output coupler transmission since the different intracavity intensity affects the pump saturation intensity, counteracting the bleaching. Figure 36a shows the absorption dependence on the incident pump power for three output couplers and also without lasing. The incident pump intensity is comparable to or exceeding the saturation intensity and since the active layer thickness is smaller than the absorption length, the effect of absorption bleaching can be clearly observed (Fig. 36a). Note that this was not the case when pumping thick bulk samples of Yb:KLuW with the same TDL. It can be seen from Fig. 36a that the bleaching effect is strongest when lasing is interrupted (in

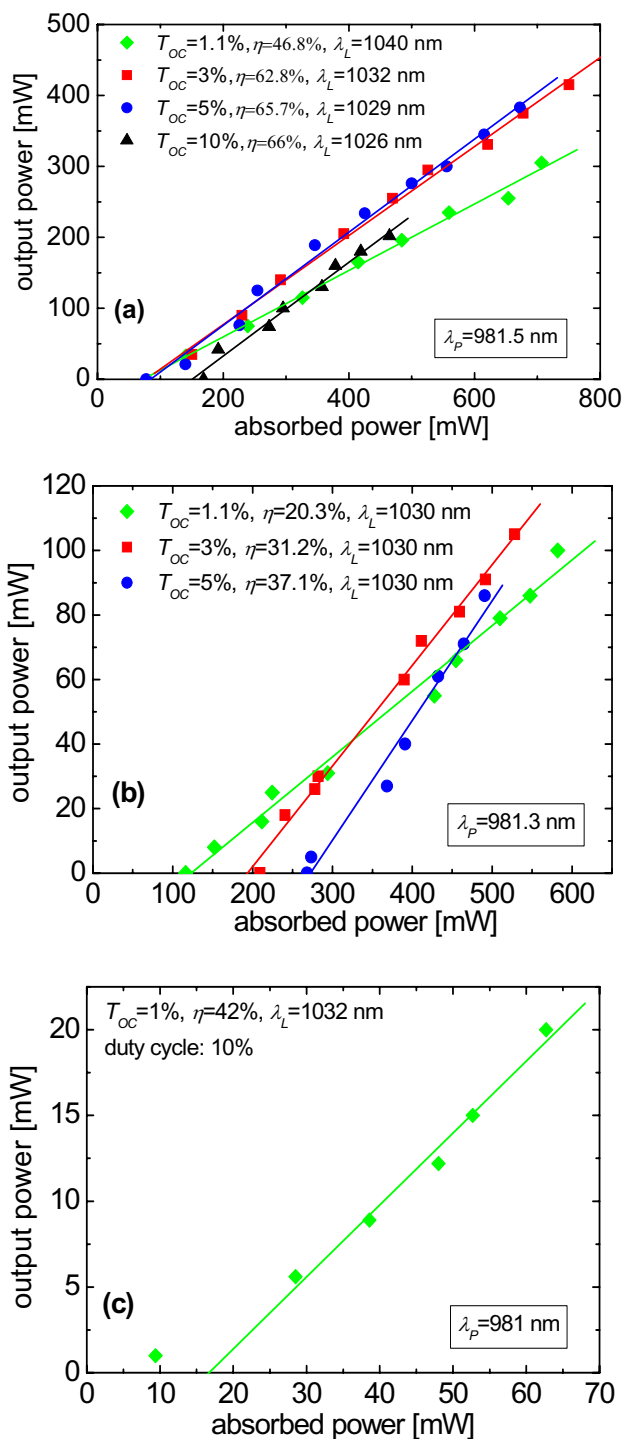


**Figure 34** Output power versus absorbed pump power for a 12 at. % Yb:KLuW epitaxy pumped in the 67 cm long cavity from Fig. 31a by the Ti:sapphire laser (a), and by the TDL (b), and quasi-CW laser performance of a 52 at. % Yb:KLuW epitaxy with Ti:sapphire laser pumping: average powers (c).

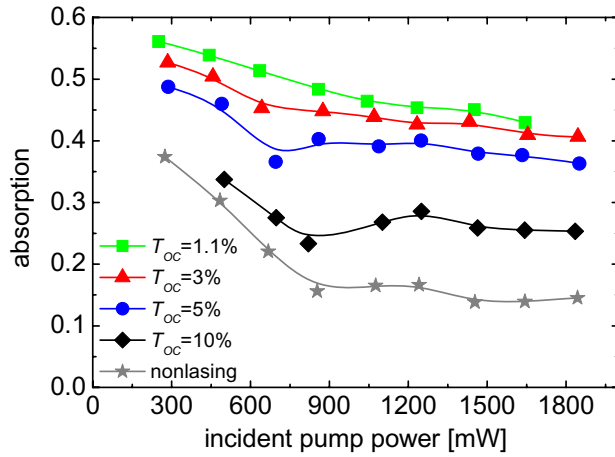


**Figure 35** Estimated single pass absorption of the Yb:KLuW/KLuW(010) epitaxy in the case of Ti:sapphire laser pumping versus incident pump power.

the M1-M2 arm in Fig. 31a). Lower transmission of the output coupler corresponds to increased intracavity intensity and consequently the absorption increases (Fig. 36b). But for a given  $T_{OC}$  the dependence on the incident pump power is not strong because the intracavity intensity also increases with increasing pump power (Fig. 36a,b).

We tested also a 52 at. % Yb:KLuW epitaxy which was cut for the same propagation and polarization directions but the doped layer was only 38  $\mu\text{m}$  thick, Fig. 34c. However, linear dependence of the input-output characteristics was obtained only using a chopper. The maximum average output power obtained was  $P_{\text{out}} = 20$  mW for an absorbed pump power of  $P_{\text{abs}} \approx 63$  mW which gives an optical-to-optical efficiency of  $\eta_0 \approx 32\%$ . The average output power obtained with the same output coupler of  $T_{OC} = 1\%$  increased to 43 mW when double-pass pumping was applied. Although the absorption of this sample was quite optimum, strong thermal effects made it very difficult to achieve true CW operation. Pumping again in the absorption maximum, in a single pass, only 17 mW of average output power at 1046.1 nm were obtained in this case for an absorbed pump power of  $P_{\text{abs}} = 250$  mW, using a special output coupler with  $T_{OC} = 0.1\%$ . For incident powers exceeding 400 mW the output quickly dropped to zero and even optical damage was observed above 500 mW. The extensive heating at high doping levels is attributed to impurities absorbing the laser and/or pump radiation which then relax non-radiatively. The influence of excitation migration to impurities can be ruled out because no substantial shortening of the fluorescence lifetime was observed for the 52 at. % Yb-doped KLuW epitaxy (Fig. 25b).

Figure 37 shows the Z-shaped cavity used for mode-locking of the Yb:KLuW lasers. Two dispersion compensating prisms could be inserted in the arm with the output coupler. The semiconductor saturable absorber mir-

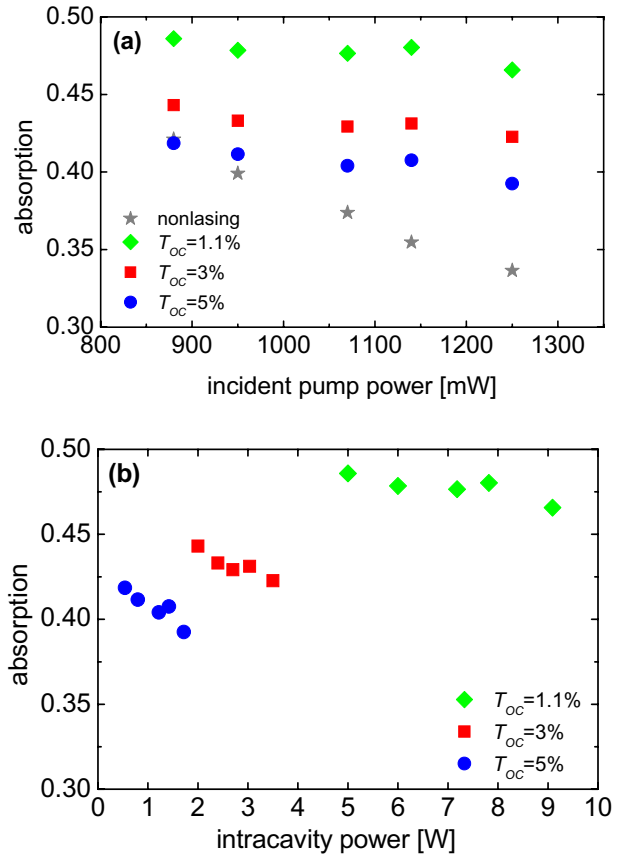


**Figure 36** Estimated single pass absorption in the case of TDL pumping of the Yb:KLuW/KLuW(010) epitaxy versus the incident pump power (a), and versus the intracavity laser power (b).

ror (SESAM) was grown by the MOCVD-method and consisted of a bottom Bragg mirror comprising 25-pairs AlAs/GaAs quarterwave layers designed for a central wavelength of 1030 nm. Its reflection band extended from 980 to 1070 nm. The 10-nm-thick InGaAs surface quantum well structure had a saturable loss of  $\approx 1\%$ . Its relaxation time was measured by the pump and probe technique to be less than 5 ps.

The same 2.8-mm thick Yb:KLuW crystal oriented for  $E//N_m$  and the 3-mm thick crystal oriented for  $E//N_p$  from the CW laser experiments, both with 6.8 at. % Yb-doping, were first compared with Ti:sapphire laser pumping, without special cooling. Without intracavity prisms, the laser operated in the picosecond regime with a pulse repetition rate of 98 MHz. Pulses as short as 2.8 ps near 1043 nm were obtained for  $E//N_p$  at a maximum average output power of  $P_{\text{out}} = 540$  mW ( $T_{OC} = 5\%$ ) corresponding to an optical-to-optical efficiency of  $\eta_0 = 32\%$ . The measured autocorrelation traces were fitted assuming a sech<sup>2</sup>-pulse shape, Fig. 38. The 13 nm broad (FWHM) spectrum indicates that the pulse duration in the picosecond mode

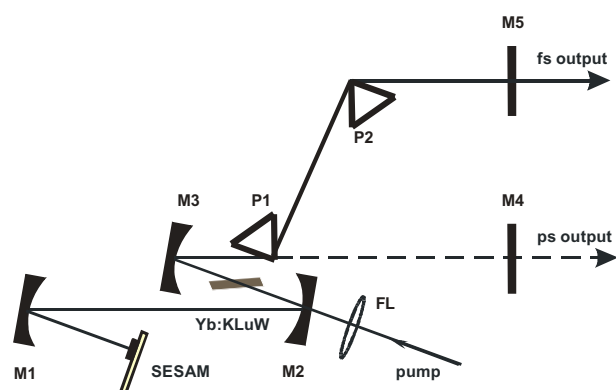


**Figure 37** Schematic of the astigmatically compensated cavity of the mode-locked Yb:KLuW laser. The folding mirrors (M1–M3) are with  $RC = -10$  cm, P1 and P2 are SF10 prisms, and FL is a lens with  $f = 6.28$  cm.

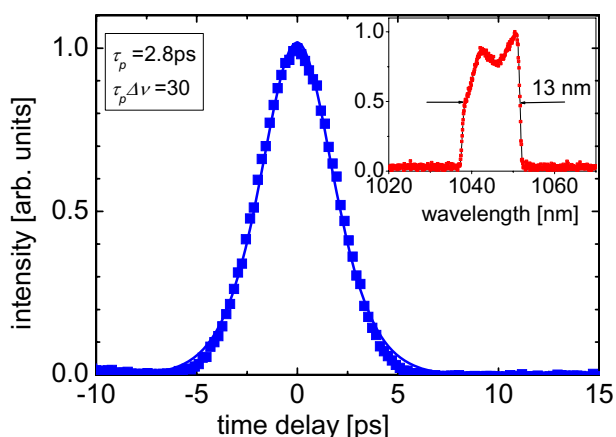


**Figure 38** Autocorrelation trace and spectrum (inset) of the Yb:KLuW laser in the picosecond regime (Ti:sapphire laser pumping).  $\tau_p$ : pulse duration (FWHM).

exceeds the Fourier limit by a factor of  $>30$ . The performance of the *b*-cut Yb:KLuW sample for  $E//N_m$  was similar in the picosecond regime.

The two SF10 Brewster prisms introduced for femtosecond operation had a tip-to-tip separation of 38 cm. The resulting pulse repetition rate was 95 MHz. The FWHM of the shortest pulse obtained for  $E//N_m$  was 81 fs (Fig. 39a), at an average output power of  $P_{\text{out}} = 70$  mW ( $T_{\text{OC}} = 3\%$ ). The corresponding spectrum was centered at 1046 nm and had a FWHM of 14.3 nm (inset Fig. 39a). This results in a time-bandwidth product of 0.318 corresponding to transform-limited  $\text{sech}^2$ -pulses. The results achieved for  $E//N_m$  and  $E//N_p$  are compared in Fig. 39b. Only minor differences can be seen, in accordance with the similar bandwidths of the calculated gain cross sections, Fig. 24. For both polarization orienta-

tions mode-locking was achieved for output couplers with transmission  $T_{\text{OC}} = 1\text{--}5\%$ . The shortest pulse duration obtained for  $E//N_p$  was 83 fs at  $\lambda_L = 1049$  nm, for an output power of  $P_{\text{out}} = 36$  mW ( $T_{\text{OC}} = 1\%$ ). Substantially higher output power,  $P_{\text{out}} = 295$  mW, was obtained for a pulse duration of 100 fs (Fig. 39b).

Using the TDL for pumping and the  $E//N_p$ -oriented Yb:KLuW crystal, stable femtosecond mode-locking was achieved for output couplers with  $T_{\text{OC}} = 1\text{--}3\%$ . A maximum output power of  $P_{\text{out}} = 56$  mW was obtained in the mode-locked regime with  $T_{\text{OC}} = 3\%$ , for an incident pump power of 1 W. The minimum pulse duration of 117 fs (FWHM) and the corresponding spectrum centered at 1053 nm (Fig. 39c) give a time-bandwidth product of 0.39, hence the generated pulses are almost Fourier-limited.

Mode-locking with the 12 at. % Yb:KLuW epitaxy was realized in the same cavity (Fig. 37) with Ti:sapphire laser pumping. In the picosecond regime, the laser operated at a repetition rate of 100 MHz, the emission spectrum was centered at 1030 nm and the FWHM of the generated pulses was 1.8 ps (Fig. 40a) assuming  $\text{sech}^2$ -pulse shape. The input-output characteristics, below and above the mode-locking threshold, are shown in Fig. 40b. The maximum output power was  $P_{\text{out}} = 119$  mW obtained with an output coupler of  $T_{\text{OC}} = 3\%$ .

The femtosecond regime was realized using an output coupler with  $T_{\text{OC}} = 1.1\%$  and a separation of 31 cm between the two intracavity prisms which resulted in a repetition rate of 101 MHz. Pulses as short as 114 fs (Fig. 40c) were generated at 1030 nm, with an average output power of 31 mW for an absorbed pump power of  $P_{\text{abs}} = 632$  mW. The time-bandwidth product (0.43) was slightly above the Fourier limit. The lower limit for the pulse duration and the observed deviation from the transform-limitation seem related to the reflection characteristics of the folding mirrors which are restricted by the close separation between the pump ( $\lambda_P$ ) and laser ( $\lambda_L$ ) wavelengths. The output power increased to  $P_{\text{out}} = 94$  mW using  $T_{\text{OC}} = 3\%$ , again at  $\lambda_L = 1030$  nm, for an absorbed power of  $P_{\text{abs}} = 671$  mW. The generated pulses had a FWHM of 200 fs in this case and were almost Fourier-limited (time-bandwidth product equal to 0.32).

The pulse durations achieved with bulk Yb:KLuW are slightly longer than the 71 fs once obtained with a Kerr-lens mode-locked Yb:KYW laser [62] but consistently shorter than the 100 fs limit reported for SESAM mode-locked Yb:KGdW and Yb:KYW lasers [63,64].

In none of the arrangements investigated, the mode-locked regime was accompanied by unwanted passive Q-switching [65] but careful alignment was necessary to suppress double or multiple pulse operation which ensured long term stable operation with an output beam basically TEM<sub>00</sub>.

For the development of composite-based femtosecond oscillators the use of epitaxial structures, where layer and substrate consist of the same crystalline material, have



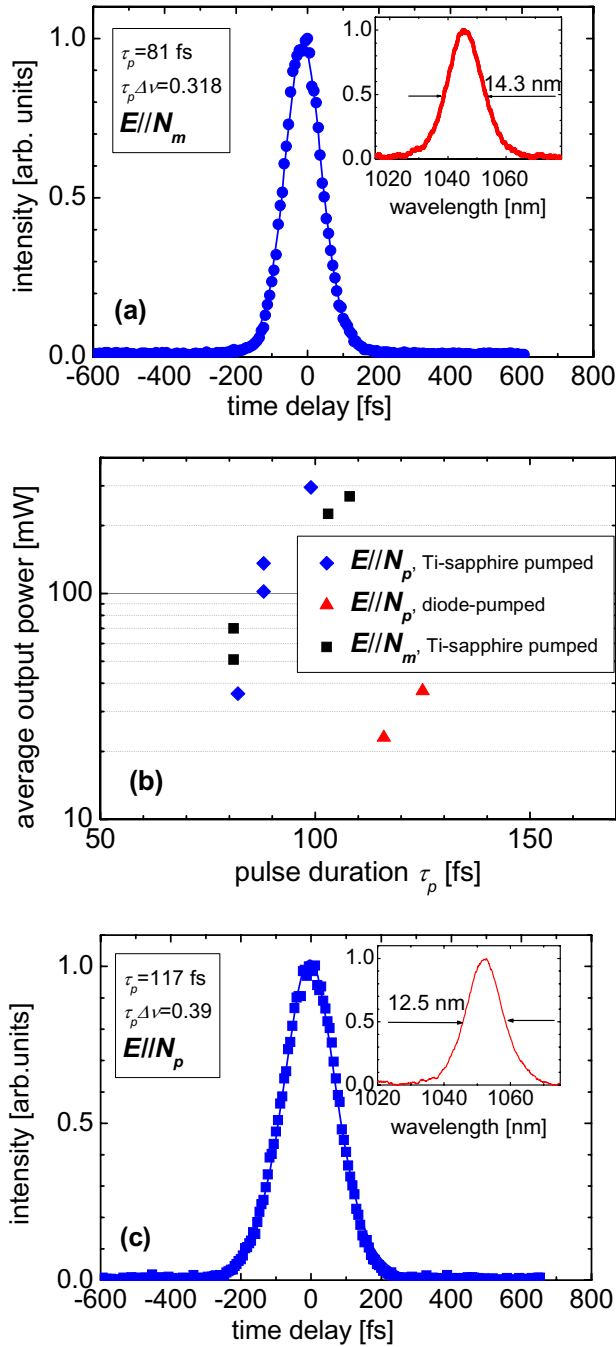


**Figure 39** Shortest pulses obtained from the Ti:sapphire laser pumped mode-locked bulk Yb:KLuW laser for  $E//N_m$  (a), comparison of the laser performance for the two polarizations  $E//N_m$  and  $E//N_p$  (b), and shortest pulses obtained with TDL pumping for  $E//N_p$  (c).  $\tau_p$ : pulse duration (FWHM);  $\tau_p \Delta\nu$ : time-bandwidth product.

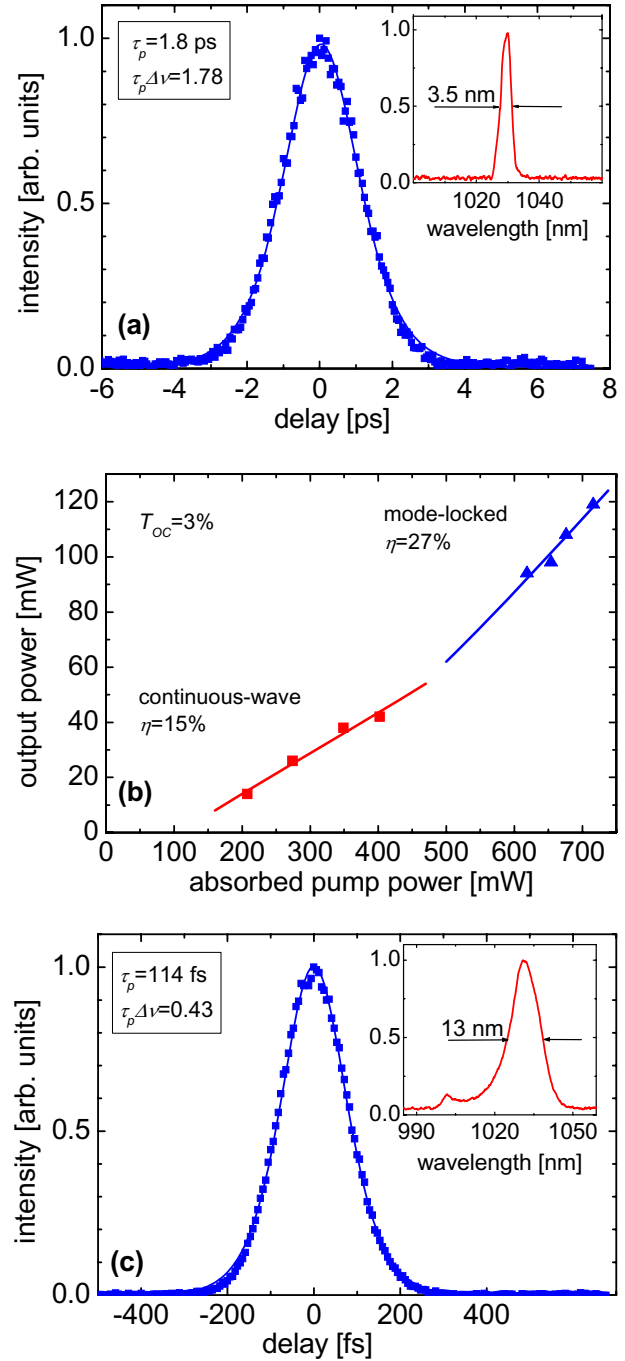


**Figure 40** Mode-locked performance of the epitaxial Yb:KLuW laser in the picosecond regime (a,b), and autocorrelation trace and spectrum in the femtosecond regime (c). In all cases the polarization is  $E//N_m$ .  $\tau_p$ : pulse duration (FWHM);  $\tau_p \Delta\nu$ : time-bandwidth product.

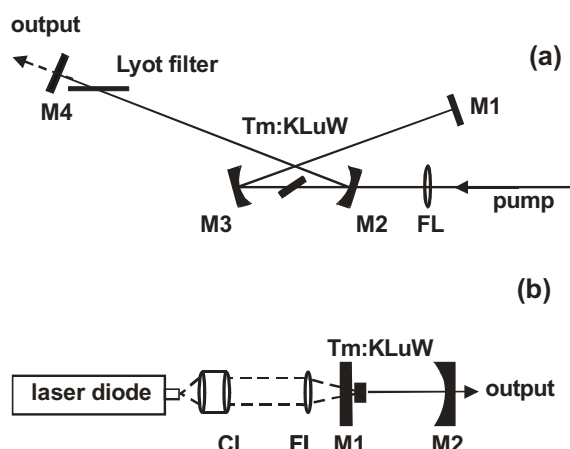


**Figure 41** Astigmatically compensated cavity of the tunable Tm:KLuW laser designed for Ti:sapphire laser pumping (a), and hemispherical cavity of the diode-pumped Tm:KLuW laser (b). In (a) the folding mirrors (M2–M3) are with  $RC = -10$  cm and FL is a lens with  $f = 7$  cm. In (b) CL and FL are collimating and focusing lens systems with  $f = 3.4$  and  $2$  cm, respectively, and the output coupler (M2) is with  $RC = -5$  cm.

essential advantages compared to hetero-composite structures like bonded crystals of Yb:YAG on sapphire [66]. They can reduce the problem of parasitic reflections and birefringence effects [67], which could strongly affect the femtosecond regime and have to be taken into consideration. Neither in the emitted spectrum nor in the field distribution of the Yb:KLuW/KLuW(010) laser could we detect any indications of modulations.

## 6. Bulk and epitaxial Tm:KLuW lasers

The 90 cm long X-type cavity shown in Fig. 41a was used for pumping of Tm:KLuW by a Ti:sapphire laser (linewidth  $\approx 0.2$  nm). For power scaling, a single 50 W commercial bar with 19 emitters (linewidth  $\approx 2$  nm) and simple adapted beam shaping optics were used with the 5 cm long cavity shown in Fig. 41b. In the position of the crystal, the pump spot had a Gaussian waist of  $37 \mu\text{m}$  (Ti:sapphire laser) and  $62 \mu\text{m}$  (diode laser).

Two bulk samples were available for pumping with the Ti:sapphire laser: They were positioned under Brewster angle which determines the laser polarization; the pump polarization was in the same plane. The maximum output power achieved with the 5 at. % Tm:KLuW sample (*b*-cut, thickness: 2 mm) without cooling, for  $E//N_m$  and  $T_{OC} = 3\%$ , was  $P_{out} = 650$  mW at a wavelength of  $\lambda_L = 1948$  nm (slope efficiency  $\eta = 60.5\%$ ). This sample absorbed 1.21 W of the incident 1.32 W. The optimum pump wavelength was  $\lambda_P = 802$  nm and the threshold ( $P_{abs}$ ) was 73 mW. The slope efficiency and the output power obtained with

**Table 14** Slope efficiency  $\eta$ , oscillation wavelength  $\lambda_L$ , and absorbed pump power at threshold in dependence on the output coupler transmission  $T_{OC}$ , for the 3.7 at. % Tm:KLuW sample.

$T_{OC}$ [%]	$\eta$ [%]		$\lambda_L$ [nm]		threshold [mW]	
	$E//N_m$	$E//N_p$	$E//N_m$	$E//N_p$	$E//N_m$	$E//N_p$
1.5	46.7	42.1	1951	1942	60	125
3	57.2	43.9	1947	1918	67	131
5	60.1	50.2	1947	1909	125	145
10	54	53.9	1917	1907	190	195

this Tm:KLuW sample were roughly 50% higher in comparison with an analogous Tm:KGdW sample [23] which can be attributed to the higher gain cross sections at the corresponding oscillation wavelengths, Fig. 29.

The 3.7 at. % Tm-doped KLuW sample (thickness: 2.92 mm) allowed to compare the two polarizations,  $E//N_m$  and  $E//N_p$ , because it had a  $N_g$ -cut. It was mounted in a Cu-block whose temperature was maintained at  $10^\circ\text{C}$  by circulating water.

The measured output power versus the absorbed power for the two polarizations and all output couplers used is shown in Fig. 42 together with the fits for calculation of the slope efficiency. The slope efficiency  $\eta$ , the oscillation wavelength  $\lambda_L$ , and the threshold (absorbed power) data are summarized in Table 14. A maximum output power of 1.4 W for an absorbed pump power of  $P_{abs} = 2.47$  W was achieved for  $E//N_m$  with the  $T_{OC} = 5\%$  output coupler. This corresponds to an optical-to-optical efficiency of  $\eta_0 = 56.7\%$  with respect to the absorbed power. The slope efficiency with respect to the absorbed power was  $\eta = 60.1\%$  and the threshold with this output coupler was 125 mW (Table 14). The absorption of the sample under lasing conditions was between 85% and 90% depending on the output coupler. The optimum pump wavelength was  $\lambda_P = 802$  nm as in the case of the 5 at. % doping which corresponds to the absorption maximum, Fig. 26. The laser wavelength varied from  $\lambda_L = 1917$  nm ( $T_{OC} = 10\%$ ) to 1951 nm ( $T_{OC} = 1.5\%$ ). For polarization  $E//N_p$ , the maximum output power achieved was slightly lower ( $P_{out} = 1.28$  W for  $T_{OC} = 10\%$ ) although the absorbed power was  $P_{abs} = 2.61$  W. The thresholds were in general slightly higher for this polarization and the slope efficiencies lower, see Table 14. The absorption of the sample for this polarization was about 95% for all output couplers. The optimum pump wavelength was  $\lambda_P = 794$  nm which corresponds to the absorption maximum for  $E//N_p$  (Fig. 26).

The higher thresholds and lower slope efficiencies for polarization  $E//N_p$  can be attributed to the lower gain cross section as could be expected from Fig. 29. The different wavelength dependence on the output coupler losses for the two polarizations is obviously related to the shapes of the gain curves as can be seen from Fig. 29. The laser wavelengths for  $E//N_p$  were always somewhat shorter.

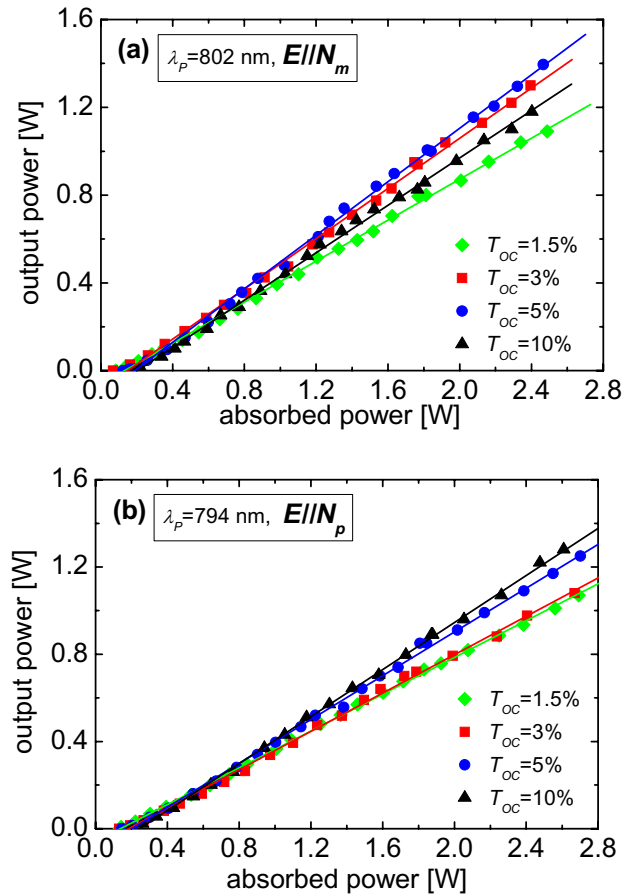


**Figure 42** Input-output laser characteristics of the 3.7 at. % Tm:KLuW sample for  $E//N_m$  (a) and  $E//N_p$  (b): In both cases the maximum incident pump power was 2.83 W.

The performance of the laser with this sample and pumping at  $\lambda_P = 802$  nm for  $E//N_p$  is interesting because this is related to the feasibility of diode pumping and the possibility to use unpolarized diode lasers for samples cut along the  $N_g$  principal axis. The slope efficiency and the threshold remained unchanged for  $E//N_p$  after moving from  $\lambda_P = 794$  nm to  $\lambda_P = 802$  nm (Fig. 43a), while the absorption obviously dropped (Fig. 43b). As can be also seen from Fig. 43b, the actual absorption remained constant independent of the incident pump power while in the absence of lasing (output mirror laser arm interrupted) it dropped from 95% to 64% in the case of  $\lambda_P = 794$  nm and from 57% to 38% in the case of  $\lambda_P = 802$  nm. This indicates that the pump saturation intensity is reduced in the lasing state and the absorption bleaching effect is suppressed. Similar dependences for the absorption were observed for all cases depicted in Fig. 42.

Tuning was studied with the 3.7 at. % Tm:KLuW sample introducing a 3-mm thick quartz plate (optical axis at  $60^\circ$  to the surface) into the long arm of the cavity (Fig. 41a). The overall tuning range extended from 1800

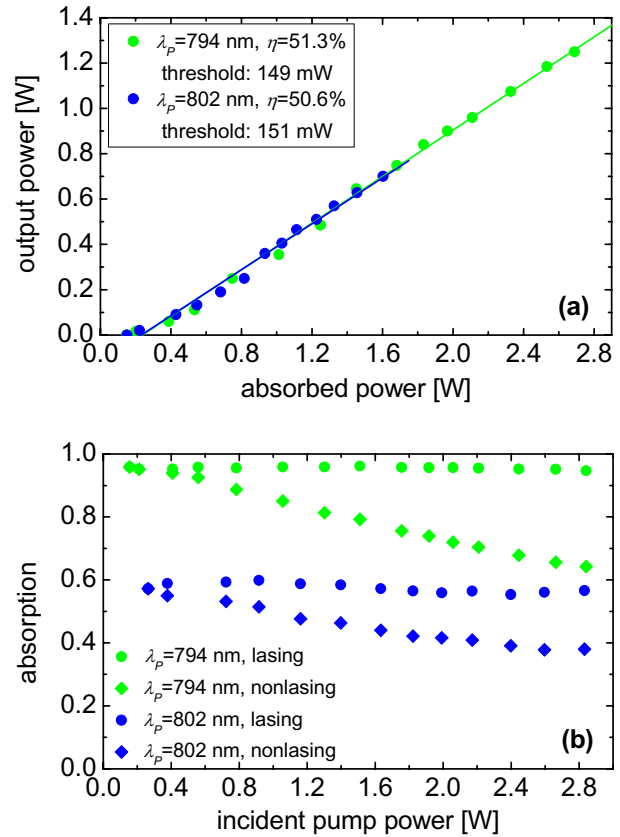


**Figure 43** Input-output characteristics (a) and absorption as a function of the incident pump power (b) of the 3.7 at. % Tm:KLuW laser ( $T_{OC} = 5\%$ ) for polarization parallel to the  $N_p$  principal optical axis and pumping at  $\lambda_P = 794$  and  $802$  nm.

to 1987 nm (Fig. 44), with FWHMs of 110 nm ( $E//N_m$ ) and 128 nm ( $E//N_p$ ). In the shorter wavelength limit the gain for  $E//N_p$  was higher, see Fig. 29.

The unpolarized diode laser pump source used for power scaling of the Tm:KLuW laser with the nearly hemispherical cavity from Fig. 41b had a maximum power of 14 W (measured behind the collimating lens) at 802 nm for an operating temperature of  $25^\circ\text{C}$ . At 20 W the wavelength was already 804.5 nm. The same 3.7 at. % Tm:KLuW sample was mounted in a Cu-holder and room temperature was maintained by water cooling. The maximum output power achieved with an output coupler of  $T_{OC} = 3\%$  was  $P_{\text{out}} = 4$  W at  $\lambda_L = 1950$  nm for an incident pump power of 15 W (Fig. 45). The slope efficiency calculated with respect to the absorbed power  $P_{\text{abs}}$  amounted to  $\eta = 69\%$  and the maximum optical-to-optical efficiency reached  $\eta_0 = 47\%$ . Having in mind the normal incidence, these efficiencies were estimated by taking into account the reflected pump light at the crystal faces (total absorption of 55%). The achieved output powers are higher in comparison to previously reported results (1.8 W) using Tm:KYW [68], obtained with a similar cavity design

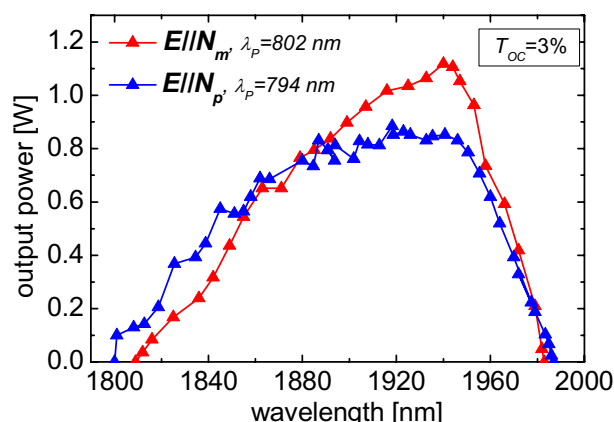


**Figure 44** Output power versus wavelength of the tunable 3.7 at. % Tm:KLuW laser for  $P_{\text{abs}} = 2.4$  W.

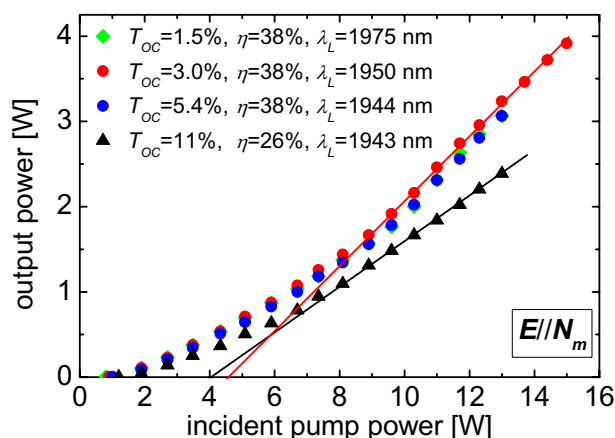


**Figure 45** Input-output characteristics of the diode-pumped bulk Tm:KLuW laser. The polarization is naturally selected.

and pump source. Also in terms of slope efficiency these results are superior if compared with the highest values previously reported with double tungstates (52–53% with Tm:KYW [68,69]) or any other Tm crystal host. Obviously the cross-relaxation mechanisms (Fig. 28) are very efficient in Tm:KLuW even at a doping level of 3.7 at. % since without this process the upper limit for  $\eta$  would be 41%.

The slope efficiencies achieved with diode pumping were higher than with Ti:sapphire laser pumping. It should be noted, however, that quite different cavities were used (Fig. 41) and the Ti:sapphire laser pumped cavity was designed for future mode-locking experiments. Nevertheless, Ti:sapphire laser pumping provided higher optical-to-optical efficiency and lower thresholds. The linear dependence of the output power for the slope efficiency in the case of diode pumping, which is practically the same

**Table 15** Slope efficiency  $\eta$ , oscillation wavelength  $\lambda_L$ , and absorbed pump power at threshold in dependence on the output coupler transmission  $T_{OC}$  for the 5.5 at. % Tm:KLuW epitaxy.

$T_{OC}$ [%]	$\eta$ [%]	$\lambda_L$ [nm]	threshold [mW]
1.5	48.5	1967	16
3	64.0	1961	20
5	60.0	1960	22

for  $T_{OC} = 1.5 \dots 5.4\%$ , is reached at higher pump levels in Fig. 45. Such behaviour is typical for quasi-four-level laser systems in the presence of reabsorption losses which increase with the crystal temperature at higher pump powers. The indicated in Fig. 45 slope efficiencies correspond to thresholds higher than the actual ones.

For a cavity without any polarization selective elements or surfaces, a crystal cut along the  $N_g$  optical axis can only naturally (by the gain cross section) select the laser polarization and this is independent of the absorption bleaching. For all output couplers and power levels the oscillating polarization of the diode-pumped Tm:KLuW laser was  $E//N_m$ .

Measurements of the output beam quality were performed at high power levels. They yielded values of the  $M^2$  parameter (deviation from the fundamental Gaussian mode) of 2.3 and 2.1 in the two planes.

A Tm:KLuW/KLuW(010) epitaxial sample with a total thickness of 1.7 mm (substrate+130  $\mu\text{m}$  thick doped layer) and actual concentration of 5.5 at. % in the layer (Table 7), mounted in a Cu-block without active cooling, was studied in the same cavity from Fig. 41a, using Ti:sapphire laser pumping. It was *b*-cut and the only possible polarization was  $E//N_m$  (Fig. 46). The pump wavelength was  $\lambda_P = 802$  nm.

A maximum output power of 78 mW was obtained for  $T_{OC} = 3\%$ . In this case, the pump power incident on the crystal was 1.23 W but the absorbed power measured under lasing conditions was only  $P_{\text{abs}} = 144$  mW. No damage was observed for the incident power applied. The results, in terms of slope efficiency (Table 15), are very similar to those obtained with the bulk 5 at. % Tm:KLuW. The output power obtained with the epitaxial sample was relatively low due to the low crystal absorption. While the calculated small-signal absorption was of the order of 24%, the absorption measured without lasing was strongly bleached and dropped to about 4%. The actual absorption under lasing conditions increased to about 15% (almost constant with the incident power). Although the laser threshold was correspondingly decreased ( $P_{\text{abs}} = 16$ –22 mW depending on  $T_{OC}$ , Table 15) in comparison to the bulk Tm:KLuW, the low crystal absorption did not allow to obtain higher output powers.

Insertion of the same Lyot filter allowed to obtain almost continuous tuning from 1894 up to 2039 nm (Fig. 47). This means a total spectral range of 145 nm with a single output coupler, the FWHM is roughly 60 nm. This re-



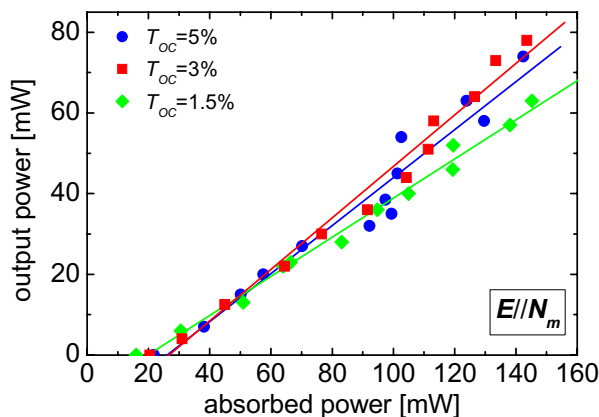


**Figure 46** Input-output characteristics of the Ti:sapphire laser pumped Tm:KLuW/KLuW(010) epitaxy.

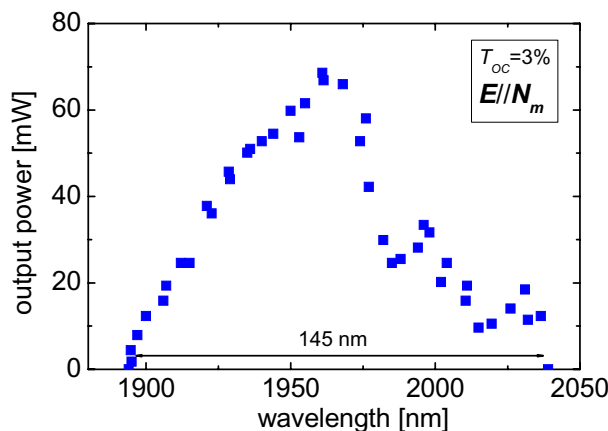


**Figure 47** Tuning of the epitaxial Tm:KLuW/KLuW(010) laser for  $T_{OC} = 3\%$  using an intracavity Lyot filter.

sult compares very well with the performance of the bulk Tm:KLuW laser, although the exact tuning range depends on the doping level, the absorption coefficient, and the output coupler.

## 7. Conclusion

Since Lu is the ion closest to Yb in the lanthanide series of the periodic table, KLuW is the most suitable host belonging to the family of the monoclinic double tungstates for Yb-doping. Besides the fact that the incorporation of Yb is easier and up to 100% doping can be achieved without affecting the quality of the grown crystals, the small lattice mismatch between KLuW and KYbW is advantageous for epitaxial growth of thin doped layers on undoped substrates. Furthermore, it is expected that the thermal conductivity of KLuW is least affected by Yb-doping.

KLuW exhibits also good mechanical properties facilitating high quality polishing and coating. The next closest active ion (radius, mass) to Lu is Tm: Hence, KLuW is also a promising host for this dopant. In contrast to Yb, the Tm-ion exhibits quenching at high doping even in the monoclinic double tungstates. Nevertheless, the other attractive features of the double tungstates, highest absorption and emission cross sections, and relatively broad bandwidths, suitable both for tuning and mode-locking, remain. Both Yb and Tm exhibit in KLuW absorption peaks which match very well the emission spectra of commercial InGaAs and AlGaAs diode lasers. This is an important prerequisite for power scaling of such lasers.

Most of the properties of the passive host crystal KLuW are now known. The spectroscopy of Yb and Tm is also well studied. While the strong anisotropy of the spectroscopic properties is in general an important advantage of KLuW for laser applications, the anisotropy of the thermo-mechanical properties can lead to some limitations. Nevertheless, precise knowledge of these properties allows to solve the problems by special design of the active elements and the thermal management schemes, including such without radial symmetry with respect to the cavity axis. Two polarizations, parallel to the  $N_m$  and  $N_p$  principal optical axes, are useful for laser operation of Yb- or Tm-doped KLuW. Both can be used for pumping, either separately or together when pumping with unpolarized diode lasers which is important for power scaling. While the gain is normally higher for  $E//N_m$ , the  $E//N_p$  polarization can have some advantages related to the spectral features (absorption or emission). The choice of any of these two polarization directions allows for more possibilities with respect to the propagation direction because KLuW is a biaxial crystal. This can be used for independent optimization of the thermal management or the nonlinear properties in the case of SRS or mode-locking (nonlinear refractive index) utilizing the anisotropy of the corresponding host parameters.

We achieved extremely high slope efficiencies for CW laser operation, both with Yb- and Tm-doped KLuW crystals, which approach the theoretical limits. In both cases diode pumping allowed to obtain multiwatt output powers. While the slope efficiencies with epitaxial composites were also rather high, there are still problems to be solved related to nonradiative, heat generating processes at high doping levels. Higher purity of the raw materials used for the flux growth process will be an important factor for the advance in this direction. Once the problem with absorbing impurities in the KLuW host is solved, it can be expected that such epitaxies could lead to a breakthrough in the thin disk laser concept reducing its geometry to a single pump pass with extremely efficient one-dimensional heat removal.

We demonstrated impressive tunability of the Tm-lasers, both bulk and epitaxial, in the 1.9- $\mu\text{m}$  spectral range. The gain bandwidths are quite large, both for Yb and Tm, which means that passive mode-locking can produce sub-100 fs light pulses. Since SESAMs are at present

available only for the 1- $\mu\text{m}$  spectral range, we were able to demonstrate this only for Yb:KLuW lasers, both bulk and epitaxial. The host KLuW is also attractive for SRS. This can be realized in a single cavity using the same doped crystal and passive Q-switching. We achieved this regime with Yb:KLuW and a saturable absorber producing sub-ns pulses at the 1<sup>st</sup> Stokes.

The future work will be focused on better heat removal through special geometries of the active elements (thin slabs or disks) as well as implementation of reflective and antireflection coatings in order to simplify the cavity design, and further scale the output power. The utilization of thermally insensitive orientations for further power scaling will require the knowledge of the thermo-optic coefficients [70]. These crystal parameters, together with the nonlinear refractive index, important for mode-locked and high power operation, are at present under study. Special coatings of the cavity mirrors are expected to allow the generation of even shorter mode-locked pulses with Yb:KLuW by supporting spectrally broader gain extending closer to the pump wavelength. This feature is characteristic for quasi-three-level laser systems where the gain bandwidth depends on the achievable inversion. The search for suitable passive elements with saturable absorption for Q-switching and mode-locking in the 1.9- $\mu\text{m}$  spectral range will also continue. Both regimes are at present under study with Tm:KLuW.

**Acknowledgements** This work was supported by the EU Project DT-CRYS (NMP3-CT-2003-505580). We also acknowledge financial support from the Spanish Government by the Projects MAT2005-06354-C03-02, MAT2004-20471-E and CIT-020400-2005-14, and from the Catalan Government by the Project 2005SGR658. We thank C. Kränkel and K. Petermann (Hamburg University, Germany) for the pinhole measurements of the lifetimes, M. Borowiec (Institute of Physics, Poland) for the specific heat measurements, M. Rico (ICMM-CSIC, Spain) for the Tm-luminescence measurements, M. Galan and G. Viera (Monocrom S.L., Spain) for the AlGaAs diode laser module used for pumping near 800 nm, G. Erbert (Ferdinand-Braun-Institut, Germany) for the TDL, and M. Zorn and M. Weyers (Ferdinand-Braun-Institute, Germany) for the SESAM used in the mode-locking experiments.



Valentin Petrov was born in Plovdiv, Bulgaria, in 1959. He received the M.Sc. degree in nuclear physics from University of Sofia, Bulgaria, in 1983, and the Ph.D. degree in optical physics from the Friedrich-Schiller-University, Jena, Germany, in 1988. He joined the Max-Born-Institute for Nonlinear Optics and Ultrafast Spectroscopy (MBI) in Berlin, Germany, in 1992. His research interests include ultrashort light pulses, laser physics, nonlinear optics, and optical materials. He has coauthored more than 180 papers in scientific journals.



Maria Cinta Pujol was born in Reus, Spain, in 1973. She received the Ph.D. degree in chemistry from University Rovira i Virgili (URV), Tarragona, Spain, in 2001 for work on the growth and characterization of lanthanide-doped monoclinic double tungstates. Since 2004 she is a member of the URV research group FiCMA (Physics and Crystallography of Materials), as a Ramon y Cajal Researcher. Currently, her research is focussed on the growth of bulk crystals and synthesis of nanocrystals of lanthanide doped materials as laser hosts, and their physical, structural and spectroscopic characterization.



Xavier Mateos received his Ph.D. degree in chemistry from University Rovira i Virgili (URV), Tarragona, Spain, in 2004. After a two year post-doctoral stay at the Max-Born-Institute for Nonlinear Optics and Ultrafast Spectroscopy, Berlin, Germany, he returned in 2007 to URV as a Tenure Track Lecturer. His current research programme is focussed on the growth and physical characterization of various laser materials.



Òscar Silvestre was born in St. Feliu de Llobregat, Spain, in 1975. He received the B. Sc. degree in Chemistry from University Rovira i Virgili (URV), Tarragona, Spain, in 2002. He is currently pursuing the Ph. D. degree at URV, focussing on Liquid Phase Epitaxial Growth of lanthanide doped monoclinic potassium double tungstates.



Simon Rivier was born in Bristol, U.K., in 1978. He received the M. Sc. degree in Micro-engineering from the Ecole Polytechnique Fédérale de Lausanne (EPFL), Switzerland, in 2003. Currently, he is working toward the Ph. D. degree at the Max-Born-Institute for Nonlinear Optics and Ultrafast Spectroscopy (MBI) in Berlin, Germany. His doctoral work is focussed on diode-pumped solid-state lasers based on three-level materials with innovative geometries for efficient mode-locked laser sources.



Magdalena Aguiló was born in Sa Pobla, Mallorca, Spain, in 1953. She received the Ph.D. degree in physics from Barcelona University, Barcelona, Spain, in 1983. Currently, she is Professor of Crystallography at University Rovira i Virgili (URV), Tarragona, Spain. Her research interests include crystal growth, X-ray diffraction, X-ray texture analysis, and physical properties related to the crystalline structure.

ray texture analysis, and physical properties related to the crystalline structure.



Rosa Maria Solé received the Ph.D. degree in physics from Barcelona University, Barcelona, Spain, in 1994. She is currently teaching applied physics at University Rovira i Virgili (URV), Tarragona, Spain. Her research interests include phase diagrams, crystal growth, and physical properties of solutions and crystals.



Junhai Liu, born in 1964, received his B.Sc., M.Sc., and Ph.D. degrees in physics from Shandong University, China, in 1984, 1990, and 1999, respectively. He started his research in the field of solid-state lasers in 1997 and his present interests are focussed on newly developed crystals doped with trivalent rare earth ions such as

Nd, Yb, Tm, etc. After stays as research fellow in the Technical University of Berlin, Germany (Oct. 2001–Feb. 2003, sponsored by the Alexander von Humboldt Foundation) and the Max-Born-Institute for Nonlinear Optics and Ultrafast Spectroscopy (MBI) in Berlin, Germany (Apr. 2004–Dec. 2006, sponsored by the European Commission), in 2007 he joined as a professor the College of Physics, Qingdao University, China.



Uwe Griebner received the Ph. D. degree in physics from the Technical University of Berlin, Germany in 1996. His Ph.D. research was on fibre bundle lasers with high average power. Since 1992 he has been with the Max-Born-Institute for Nonlinear Optics and Ultrafast Spectroscopy (MBI) in Berlin, Germany, working on diode

pumped solid-state lasers, fibre lasers, waveguide lasers, microoptics, microoptics for special resonators, and ultrafast lasers. He is currently focussed on ultrafast diode-pumped solid-state lasers and amplifiers.



Francesc Díaz was born in Lugo, Spain, in 1953. He received the Ph. D. degree in physics from Barcelona University, Barcelona, Spain, in 1982. Currently, he is Professor of Applied Physics at the University Rovira i Virgili (URV), Tarragona, Spain. His research interests include nanostructuring of optical materials, spectroscopy of rare-earth ions for laser applications, and nonlinear optical processes.

## References

- [1] P.V. Klevtsov and L.P. Kozeeva, Synthesis and X-ray and thermal studies of potassium rare-earth tungstates,  $\text{KLn}(\text{WO}_4)_2$ , Ln = rare-earth element, *Sov. Phys. - Dokl.* **14**, 185–187 (1969) [transl. from *Dokl. Akad. Nauk SSSR* **185**, 571–574 (1969)].
- [2] A.A. Kaminskii, K. Ueda, H.E. Eichler, J. Findeisen, S.N. Bagaev, F.A. Kuznetsov, A. A. Pavlyuk, G. Boulon, and F. Bourgeois, Monoclinic tungstates  $\text{K Dy}(\text{WO}_4)_2$  and  $\text{K Lu}(\text{WO}_4)_2$ : New  $\chi^{(3)}$ -active crystals for laser Raman shifters, *Jpn. J. Appl. Phys.* **37**, L923–L926 (1998).
- [3] J. Hanuza and L. Macalik, Polarized infra-red and Raman spectra of monoclinic  $\alpha\text{-KLn}(\text{WO}_4)_2$  single crystals (Ln = Sm–Lu, Y), *Spectrochimica Acta* **43A**, 361–373 (1987).
- [4] A.A. Kaminskii, A.A. Pavlyuk, N.R. Agamalyan, L.I. Bobovich, A.V. Lukin, and V.V. Lyubchenko, Stimulated emission by  $\text{K Lu}(\text{WO}_4)_2\text{-Er}^{3+}$  crystals at room temperature, *Inorg. Mater.* **15**, 1182–1183 (1979) [transl. from *Izv. Akad. Nauk SSSR, Neorganicheskie Materialy* **15**, 1496–1497 (1979)].
- [5] T.S. Avsievich, V.N. Verenik, A.A. Pavlyuk, R.A. Puko, A.P. Shkadarevich, and V.D. Yarzhemkovskii, Kinetics of the luminescence of the  $\text{Ho}^{3+}$  ion  $\text{KA}'(\text{WO}_4)_2$  crystals, *J. Appl. Spectr.* **44**, 248–251 (1986) [transl. from *Zhurnal Prikladnoi Spektroskopii* **44**, 407–410 (1986)].
- [6] A.A. Kaminskii, A.G. Petrosyan, V.A. Fedorov, S.E. Sarkisov, V.V. Ryabchenkov, A.A. Pavlyuk, V.V. Lyubchenko, and I.V. Mochalov, Two-micron stimulated emission by crystals with  $\text{Ho}^{3+}$  ions, based on



- the transition  $^5\text{I}_7 \rightarrow ^5\text{I}_8$ , *Sov. Phys. - Dokl.* **26**, 846–848 (1981) [transl. from *Dokl. Akad. Nauk SSSR* **260**, 64–67 (1981)].
- [7] A.A. Kaminskii, A.A. Pavlyuk, N.R. Agamalyan, S.E. Sarkisov, L.I. Bobovich, A.V. Lukin, and V.V. Lyubchenko, Stimulated radiation of  $\text{Nd}^{3+}$  and  $\text{Ho}^{3+}$  ions in monoclinic  $\text{KLu}(\text{WO}_4)_2$  crystals at room temperature, *Inorg. Mater.* **15**, 1649 (1979) [transl. from *Izv. Akad. Nauk SSSR, Neorganicheskie Materialy* **15**, 2092 (1979)].
- [8] A.A. Kaminskii, N.R. Agamalyan, A.A. Pavlyuk, L.I. Bobovich, and V.V. Lyubchenko, Preparation and luminescence-generation properties of  $\text{KLu}(\text{WO}_4)_2$ - $\text{Nd}^{3+}$ , *Inorg. Mater.* **19**, 885–894 (1983) [transl. from *Izv. Akad. Nauk SSSR, Neorganicheskie Materialy* **19**, 982–991 (1983)].
- [9] A.A. Kaminskii, A.I. Bodretsova, A.G. Petrosyan, and A.A. Pavlyuk, New quasi-CW pyrotechnically pumped crystal lasers, *Sov. J. Quantum Electron.* **13**, 975–976 (1983) [transl. from *Kvantovaya Elektron. (Moscow)* **10**, 1493–1494 (1983)].
- [10] A.A. Kaminskii, H.R. Verdun, W. Koechner, F.A. Kuznetsov, and A.A. Pavlyuk, Efficient single-mode cw lasers based on monoclinic double potassium-(rare earth) tungstate crystals containing  $\text{Nd}^{3+}$  ions with semiconductor-laser pumping, *Sov. J. Quantum Electron.* **22**, 875–877 (1992) [transl. from *Kvantovaya Elektron. (Moscow)* **19**, 941–943 (1992)].
- [11] L. Tang, Z. Lin, Z. Hu, and G. Wang, Growth and spectral properties of  $\text{Nd}^{3+}:\text{KLu}(\text{WO}_4)_2$  crystal, *J. Cryst. Growth* **277**, 228–232 (2005).
- [12] L. Tang and G. Wang, Spectral parameters of  $\text{Nd}^{3+}$  ion in  $\text{Nd}^{3+}:\text{KLu}(\text{WO}_4)_2$  crystal, *Chinese J. Struct. Chem.* **23**, 383–386 (2005).
- [13] J. Zhang, J. Wang, H. Zhang, F. Xu, Z. Wang, Z. Shao, H. Zhao, and Y. Wang, Growth and diode-pumped CW lasing of  $\text{Nd}:\text{KLu}(\text{WO}_4)_2$ , *J. Cryst. Growth* **284**, 108–111 (2005).
- [14] L.I. Yudanov, O.G. Potapova, and A.A. Pavlyuk, Phase diagram of the system  $\text{KLu}(\text{WO}_4)_2$ - $\text{KNd}(\text{WO}_4)_2$  and growth of  $\text{KLu}(\text{WO}_4)_2$  single crystals, *Inorg. Mater.* **23**, 1657–1660 (1987) [transl. from *Izv. Akad. Nauk SSSR, Neorganicheskie Materialy* **23**, 1884–1887 (1987)].
- [15] X. Mateos, V. Petrov, M. Aguiló, R.M. Sole, J. Gavalda, J. Massons, F. Diaz, and U. Griebner, Continuous-wave laser oscillation of  $\text{Yb}^{3+}$  in monoclinic  $\text{KLu}(\text{WO}_4)_2$ , *IEEE J. Quantum Electron.* **40**, 1056–1059 (2004).
- [16] X. Mateos, R. Sole, J. Gavalda, M. Aguiló, J. Massons, F. Diaz, V. Petrov, and U. Griebner, Crystal growth, spectroscopic studies and laser operation of  $\text{Yb}^{3+}$ -doped potassium lutetium tungstate, *Opt. Mat.* **28**, 519–523 (2006).
- [17] J. Liu, U. Griebner, V. Petrov, H. Zhang, J. Zhang, and J. Wang, Efficient continuous-wave and Q-switched operation of a diode-pumped  $\text{Yb}:\text{KLu}(\text{WO}_4)_2$  laser with self-Raman conversion, *Opt. Lett.* **30**, 2427–2429 (2005).
- [18] U. Griebner, S. Rivier, V. Petrov, M. Zorn, G. Erbert, M. Weyers, X. Mateos, M. Aguiló, J. Massons, and F. Diaz, Passively mode-locked  $\text{Yb}:\text{KLu}(\text{WO}_4)_2$  oscillators, *Opt. Exp.* **13**, 3465–3470 (2005).
- [19] U. Griebner, J. Liu, S. Rivier, A. Aznar, R. Grunwald, R.M. Sole, M. Aguiló, F. Diaz, and V. Petrov, Laser operation of epitaxially grown  $\text{Yb}:\text{KLu}(\text{WO}_4)_2$ - $\text{KLu}(\text{WO}_4)_2$  composites with monoclinic crystalline structure, *IEEE J. Quantum Electron.* **41**, 408–414 (2005).
- [20] V. Petrov, S. Rivier, U. Griebner, J. Liu, X. Mateos, A. Aznar, R. Sole, M. Aguiló, and F. Diaz, Epitaxially grown  $\text{Yb}:\text{KLu}(\text{WO}_4)_2$  composites for continuous-wave and mode-locked lasers in the 1  $\mu\text{m}$  spectral range, *J. Non-Cryst. Sol.* **352**, 2367–2370 (2006).
- [21] S. Rivier, X. Mateos, V. Petrov, U. Griebner, A. Aznar, O. Silvestre, R. Sole, M. Aguiló, F. Diaz, M. Zorn, and M. Weyers, Mode-locked laser operation of epitaxially grown  $\text{Yb}:\text{KLu}(\text{WO}_4)_2$  composites, *Opt. Lett.* **30**, 2484–2486 (2005).
- [22] V. Petrov, J. Liu, M. Galan, G. Viera, C. Pujol, U. Griebner, M. Aguiló, and F. Diaz, Efficient diode-pumped cw  $\text{Tm}:\text{KLu}(\text{WO}_4)_2$  laser, *Proc. SPIE* **6216**, 161–170 (2006).
- [23] X. Mateos, V. Petrov, J. Liu, M.C. Pujol, U. Griebner, M. Aguiló, F. Diaz, M. Galan, and G. Viera, Efficient 2- $\mu\text{m}$  continuous-wave laser oscillation of  $\text{Tm}^{3+}:\text{KLu}(\text{WO}_4)_2$ , *IEEE J. Quantum Electron.* **42**, 1008–1015 (2006).
- [24] O. Silvestre, M.C. Pujol, M. Aguiló, F. Diaz, X. Mateos, V. Petrov, and U. Griebner, CW laser operation of  $\text{KLu}_{0.945}\text{Tm}_{0.055}(\text{WO}_4)_2$ - $\text{KLu}(\text{WO}_4)_2$  epilayers near 2- $\mu\text{m}$ , *IEEE J. Quantum Electron.* **43**, 257–260 (2007).
- [25] P.V. Klevtsov, L.P. Kozeeva, and L.Yu. Kharchenko, Study of the crystallization and polymorphism of double potassium and trivalent metal tungstates,  $\text{KR}(\text{WO}_4)_2$ , *Sov. Phys. Crystallogr.* **20**, 732–735 (1975) [transl. from *Kristallografiya* **20**, 1210–1215 (1975)].
- [26] K. Wang, J. Zhang, J. Wang, W. Yu, H. Zhang, Z. Wang, and Z. Shao, Spectral and luminescent properties of trivalent samarium ions in  $\text{KLu}(\text{WO}_4)_2$  crystals, *Mat. Res. Bull.* **41**, 1695–1700 (2006).
- [27] J. Wang, H. Zhang, Z. Wang, W. Ge, J. Zhang, and M. Jiang, Growth, properties and Raman shift laser in tungstate crystals, *J. Cryst. Growth* **292**, 377–380 (2006).
- [28] H. Zhao, J. Wang, J. Li, H. Zhang, J. Zhang, Z. Ling, H. Xia, and R.I. Boughton, Optical and thermal properties of crystalline  $\text{Tb}:\text{KLu}(\text{WO}_4)_2$ , *Materials Letters* **61**, 2499–2501 (2007).
- [29] H. Zhao, J. Wang, J. Li, J. Zhang, H. Zhang, and M. Jiang, Growth, optical and thermal properties of  $\text{Yb}:\text{Tm}:\text{KLu}(\text{WO}_4)_2$ , *J. Cryst. Growth* **293**, 223–227 (2006).
- [30] M.C. Pujol, X. Mateos, A. Aznar, X. Solans, S. Surinach, J. Massons, F. Diaz, and M. Aguiló, Structural redetermination, thermal expansion and refractive indices of  $\text{KLu}(\text{WO}_4)_2$ , *J. Appl. Cryst.* **39**, 230–236 (2006).
- [31] J. Zhang, J. Wang, K. Wang, W. Yu, H. Zhang, Z. Wang, X. Wang, and M. Ba, Growth and structure of monoclinic  $\text{KLu}(\text{WO}_4)_2$  crystals, *J. Cryst. Growth* **292**, 373–376 (2006).
- [32] M.C. Pujol, M. Sole, J. Massons, J. Gavalda, X. Solans, C. Zaldo, F. Diaz, and M. Aguiló, Structural study of monoclinic  $\text{KGd}(\text{WO}_4)_2$  and effects of lanthanide substitution, *J. Appl. Cryst.* **34**, 1–6 (2001).
- [33] O. Silvestre, M.C. Pujol, M. Rico, F. Güell, M. Aguiló, and F. Diaz, Thulium doped monoclinic  $\text{KLu}(\text{WO}_4)_2$  single crystals: growth and spectroscopy, *Appl. Phys. B* (2007), in press.



- [34] L. Macalik, P.J. Deren, J. Hanuza, W. Strek, A.A. Demidovich, and A.N. Kuzmin, Effect of random distribution and molecular interactions on optical properties of  $\text{Er}^{3+}$  dopant in  $\text{KY}(\text{WO}_4)_2$  and  $\text{Ho}^{3+}$  in  $\text{KYb}(\text{WO}_4)_2$ , *J. Mol. Struct.* **450**, 179–192 (1998).
- [35] L. Macalik, J. Hanuza, and A.A. Kaminskii, Polarized infrared and Raman spectra of  $\text{KGd}(\text{WO}_4)_2$  and their interpretation based on normal coordinate analysis, *J. Raman Spect.* **33**, 92–103 (2002).
- [36] M.C. Pujol, M.A. Bursukova, F. Güell, X. Mateos, R. Solé, Jna. Gavalda, M. Aguiló, J. Massons, F. Díaz, P. Klopp, U. Griebner, and V. Petrov, Growth, optical characterization, and laser operation of a stoichiometric crystal  $\text{KYb}(\text{WO}_4)_2$ , *Phys. Rev. B* **65**, 165121–1–11 (2002).
- [37] Z.C. Ling, H.R. Xia, S.Q. Sun, D.G. Ran, F.Q. Liu, P. Zhao, C.Y. Gao, J.X. Zhang, J.Y. Wang, Lattice vibration and thermal diffusion of Yb doped  $\text{KLu}(\text{WO}_4)_2$  single crystal, *J. Appl. Phys.* **100**, 043522–1–6 (2006).
- [38] P.V. Klevtsov, L.P. Kozeeva, L. Lu. Kharchenko, and A.A. Pavlyuk, Polymorphism of  $\text{KY}(\text{WO}_4)_2$  and isostructural potassium-rare earth tungstates, *Sov. Phys. Crystallogr.* **19**, 342–346 (1974) [transl. from *Kristallografiya* **19**, 552–559 (1974)].
- [39] P.V. Klevtsov and R.F. Klevtsova, Polymorphism of the double molybdates and tungstates of mono- and trivalent metals with the composition  $\text{M}^+\text{R}^{3+}(\text{EO}_4)_2$ , *J. Struct. Chem.* **18**, 339–355 (1977) [transl. from *Zhurnal Strukturnoi Khimii* **18**, 419–439 (1977)].
- [40] J. Zhang, K. Wang, J. Wang, H. Zhang, W. Yu, X. Wang, Z. Wang, Q. Lu, M. Ba, D.G. Ran, Z.C. Ling, and H.R. Xia, Anisotropic thermal properties of monoclinic  $\text{Yb:KLu}(\text{WO}_4)_2$  crystals, *Appl. Phys. Lett.* **87**, 061104–1–3 (2005).
- [41] R. Sole, V. Nikolov, X. Ruiz, Jna. Gavalda, X. Solans, M. Aguiló, and F. Diaz, Growth of  $\beta\text{-KGd}_{1-x}\text{Nd}_x(\text{WO}_4)_2$  single crystals in  $\text{K}_2\text{W}_2\text{O}_7$  solvents, *J. Cryst. Growth* **169**, 600–603 (1996).
- [42] M.C. Pujol, X. Mateos, M. Sole, J. Massons, Jna. Gavalda, X. Solans, F. Diaz, and M. Aguiló, Structure, crystal growth and physical anisotropy of  $\text{KYb}(\text{WO}_4)_2$ , a new laser matrix, *J. Appl. Cryst.* **35**, 108–112 (2002).
- [43] P. Hartman and W.G. Perdok, On the relations between structure and morphology of crystal, *Acta Cryst.* **8**, 49–52 (1955).
- [44] K. Wang, J. Zhang, J. Wang, W. Yu, H. Zhang, Z. Wang, X. Wang, and M. Ba, Predicted and real habits of flux grown potassium lutetium tungstate single crystals, *Crystal Growth & Design* **5**, 1555–1558 (2005).
- [45] K. Wang, J. Zhang, J. Wang, W. Yu, H. Zhang, Z. Wang, and M. Ba, Investigation of growth mechanisms of TSS-grown  $\text{KLu}(\text{WO}_4)_2$  crystals by atomic force microscopy, *Opt. Mat.* **29**, 421–424 (2006).
- [46] K. Wang, J. Zhang, J. Wang, W. Yu, H. Zhang, and Z. Wang, Periodic transition of microcrystals on the host (110) face of  $\text{KLu}(\text{WO}_4)_2$  crystals, *J. Appl. Cryst.* **38**, 975–978 (2005).
- [47] S.B. Ubizskii, A.O. Matkovskii, S.S. Melnyk, I.M. Syvorotka, V. Müller, V. Peters, K. Petermann, A. Beyertt, and A. Giesen, Optical properties of epitaxial YAG:Yb films, *phys. stat. sol. (a)* **201**, 791–797 (2004).
- [48] Y. Jiang, K. Wang, X. Wang, C. Jia, J. Zhang, J. Wang, H. Ma, R. Nie, and D. Shen, Optical waveguide formed in  $\text{Yb:KLu}(\text{WO}_4)_2$  crystal by 6.0 MeV  $\text{O}^+$  implantation, *Chin. Phys. Lett.* **23**, 922–924 (2006).
- [49] A. Aznar, O. Silvestre, M.C. Pujol, R. Sole, M. Aguiló, and F. Diaz, Liquid-phase epitaxy crystal grown of monoclinic  $\text{KLu}_{1-x}\text{Yb}_x(\text{WO}_4)_2/\text{KLu}(\text{O}_4)_2$  layers, *Cryst. Growth & Design* **6**, 1781–1787 (2006).
- [50] K. Wang, J. Zhang, J. Wang, H. Zhang, Z. Wang, W. Yu, X. Wang, Q. Lu, and M. Ba, Anisotropic thermal expansion of monoclinic potassium lutetium tungstate single crystals, *J. Appl. Phys.* **98**, 046101–1–3 (2005).
- [51] M.C. Pujol, X. Mateos, R. Sole, J. Massons, Jna. Gavalda, F. Diaz, and M. Aguiló, linear thermal expansion tensor in  $\text{KRE}(\text{WO}_4)_2$  ( $\text{RE} = \text{Gd}, \text{Y}, \text{Er}, \text{Yb}$ ) monoclinic crystals, *Mater. Sci. Forum* **378–381**, 710–715 (2001).
- [52] L.D. Deloach, S.A. Payne, L.L. Chase, L.K. Smith, W.L. Kway, and W.F. Krupke, Evaluation of absorption and emission properties of  $\text{Yb}^{3+}$  doped crystals for laser applications, *IEEE J. Quantum Electron.* **29**, 1179–1191 (1993).
- [53] A.A. Lagatsky, N.V. Kuleshov, and V.P. Mikhailov, Diode pumped CW lasing of  $\text{Yb:KYW}$  and  $\text{Yb:KGW}$ , *Opt. Commun.* **165**, 71–75 (1999).
- [54] N.V. Kuleshov, A.A. Lagatsky, A.V. Podlipensky, V.P. Mikhailov, and G. Huber, Pulsed laser operation of Yb-doped  $\text{KY}(\text{WO}_4)_2$  and  $\text{KGd}(\text{WO}_4)_2$ , *Opt. Lett.* **22**, 1317–1319 (1997).
- [55] K. Petermann, D. Fagundes-Peters, J. Johannsen, M. Mond, V. Peters, J.J. Romero, S. Kutovoi, J. Speiser, and A. Giesen, Highly Yb-doped oxides for thin disc lasers, *J. Cryst. Growth* **275**, 135–140 (2005).
- [56] F. Güell, Jna. Gavalda, R. Sole, M. Aguiló, F. Diaz, M. Galan, and J. Massons, 1.48 and 1.84  $\mu\text{m}$  thulium emissions in monoclinic  $\text{KGd}(\text{WO}_4)_2$  single crystals, *J. Appl. Phys.* **95**, 919–923 (2004).
- [57] S.N. Bagaev, S.M. Vatnik, A.P. Maiorov, A.A. Pavlyuk, and D.V. Plakushchev, The spectroscopy and lasing of monoclinic  $\text{Tm:KY}(\text{WO}_4)_2$ , *Quantum Electron.* **30**, 310–314 (2000) [transl. from *Kvantovaya Elektronika* **30**, 310–314 (2000)].
- [58] M.C. Pujol, F. Güell, X. Mateos, Jna. Gavalda, R. Solé, J. Massons, M. Aguiló, F. Díaz, G. Boulon, and A. Brenier, Crystal growth and spectroscopic characterization of  $\text{Tm}^{3+}$ -doped  $\text{KYb}(\text{WO}_4)_2$  single crystals, *Phys. Rev. B* **66**, 144304–1–8 (2002).
- [59] A. Lagatsky, A. Abdolvand, and N.V. Kuleshov, Passive Q switching and self-frequency Raman conversion in a diode-pumped  $\text{Yb:KGd}(\text{WO}_4)_2$  laser, *Opt. Lett.* **25**, 616–618 (2000).
- [60] A.S. Grabtchikov, A.N. Kuzmin, V.A. Lisinetskii, V.A. Orlovich, A.A. Demidovich, M.B. Danailov, H.J. Eichler, A. Bednarkiewicz, W. Strek, and A.N. Titov, Laser operation and Raman self-frequency conversion in  $\text{Yb:KYW}$  microchip laser, *Appl. Phys. B* **75**, 795–797 (2002).
- [61] N. Kuleshov, V. Kisel, and V. Shcherbitsky, Efficient self-frequency Raman conversion in a passively Q-switched diode-pumped  $\text{KGd}(\text{WO}_4)_2$  laser, *OSA Trends in Optics and Photonics (TOPS) vol. 83, Advanced Solid-State Photonics*, (Optical Society of America, Washington, D.C., 2003), pp. 189–192.

- [62] H. Liu, J. Nees, and G. Mourou, Diode-pumped Kerr-lens mode-locked Yb:KY(WO<sub>4</sub>)<sub>2</sub> laser, *Opt. Lett.* **26**, 1723–1725 (2001).
- [63] G. Paunescu, J. Hein, and R. Sauerbrey, 100-fs diode-pumped Yb:KGW mode-locked laser, *Appl. Phys. B* **79**, 555–558 (2004).
- [64] P. Klopp, V. Petrov, U. Griebner, and G. Erbert, Passively mode-locked Yb:KYW laser pumped by a tapered diode laser, *Opt. Exp.* **10**, 108–113 (2002).
- [65] C. Hönniger, R. Paschotta, F. Morier-Genoud, M. Moser, and U. Keller, *Q*-switching stability limits of continuous-wave passive mode locking, *J. Opt. Soc. Am. B* **16**, 46–56 (1999).
- [66] C. L. Bonner, T. Bhutta, D. P. Shephard, and A. C. Tropper, Double-clad structures and proximity coupling for diode-bar-pumped planar waveguide lasers, *IEEE J. Quantum Electron.* **36**, 236–242 (2000).
- [67] F. Krausz, M. E. Fermann, T. Brabec, P. F. Curley, M. Hofer, M. H. Ober, C. Spielmann, E. Wintner, and A. J. Schmidt, Femtosecond Solid-State Lasers, *IEEE J. Quantum Electron.* **28**, 2097–2121 (1992).
- [68] L. E. Batay, A. A. Demidovich, A. N. Kuzmin, A. N. Titov, M. Mond, and S. Kück, Efficient tunable laser operation of diode-pumped Yb, Tm:KY(WO<sub>4</sub>)<sub>2</sub> around 1.9 μm, *Appl. Phys. B* **75**, 457–461 (2002).
- [69] A. E. Troshin, V. E. Kisel, V. G. Shcherbitsky, N. V. Kuleshov, A. A. Pavlyuk, E. B. Dunina, and A. A. Kornienko, Laser performance of Tm:KY(WO<sub>4</sub>)<sub>2</sub> crystal, *OSA Trends in Optics and Photonics (TOPS) vol. 98, Advanced Solid-State Photonics (Optical Society of America, Washington, DC 2005)*, pp. 214–218.
- [70] J. E. Hellström, S. Bjurshagen, V. Pasiskevicius, Laser performance and thermal lensing in high-power diode pumped Yb:KGW with athermal orientation, *Appl. Phys. B* **83**, 55–59 (2006).